Propagation and Beam Geometry Effects on Two-Dimensional Fourier Transform Spectra of Multilevel Systems†

Byungmoon Cho, Michael K. Yetzbacher,‡ Katherine A. Kitney, Eric R. Smith,§ and David M. Jonas*

Department of Chemistry and Biochemistry, University of Colorado, Boulder, Colorado 80309-0215

Received: May 14, 2009; Revised Manuscript Received: August 27, 2009

Four-level two-dimensional (2D) Fourier transform relaxation spectra are simulated with response functions for a chromophore pair in the exponential relaxation (optical Bloch model) limit. The parameters in this study are chosen to model coupled carbonyl stretching vibrations. As long as coherence persists, every peak in the real 2D spectra has a partially mixed absorptive/dispersive ("phase-twisted") shape because the nonlinear signals are not symmetric with respect to interchange of the first two pulses. This asymmetry in 2D relaxation spectra arises from coherence between singly excited states and a red shift of the doubly excited state. Coherence between the singly excited states causes oscillation of the 2D spectra and the associated spectrally resolved pump−probe (SRPP) transients at the quantum beat frequency. Projecting the phase-twisted nature of the 2D peaks onto the detection frequency axis, the SRPP peaks are also asymmetric about their maximum when not at maximum or minimum amplitude. Three-dimensional Fourier transform (3DFT) methods are used to simulate absorption/dispersion and beam geometry distortions of the multilevel 2D spectra with cross peaks. The distortions can be understood by consideration of their effects on individual coherence pathways that contribute to peaks in the 2D spectra. The beam geometry distortion explains some unequal cross peak amplitudes previously observed experimentally by Khalil et al. (*J. Chem. Phys.* **2004**, *121*, 362). A representation of 2D spectra that reduces beam geometry distortion is presented. If the transformation to correct for beam geometry distortion is combined with the transformations that correct absorptive/dispersive propagation distortions (*J. Chem. Phys.* **2007**, *126*, 044511), the recovered 2D spectrum matches the ideal 2D spectrum after all coherence is destroyed. In the presence of coherence, the new representation reduces the error in the distorted 2D spectrum by a factor of 4 for practical 2D-IR experimental conditions.

I. Introduction

Multidimensional Fourier transform methods in nuclear magnetic resonance (NMR) spectroscopy have proven to be enormously powerful[1,2] because of their ability to separate overlapping peaks by spreading them out in additional dimensions, correlate coupled transitions through cross peaks, and map excitation transfer pathways and measure rates by following the growth of new cross peaks. With coherent femtosecond excitation, much progress has been made in extending the same methods used in NMR to the faster dynamics probed in electronic and vibrational spectroscopy.[3–16] In two-dimensional Fourier transform (2DFT) spectra, the ability to map out linked transitions via cross peaks opens up the possibility of structural studies with femtosecond time resolution. At large relaxation times, the information content of the 2D spectra treated here becomes identical to optical−optical double resonance.[17] However, the conceptual basis for coherent nonlinear optics[18] traces its roots to nonlinear NMR.[2] Still, much of the theory developed for 2D NMR requires modification for application to the optical range.[19–23] In the optical regime, strongly absorbing samples are sometimes experimentally necessary, making it important to understand propagation effects, which can strongly reshape femtosecond excitation fields and signal fields.[6] Warren and co-workers[24,25] first simulated propagation distortions on collinear 2D optical spectra of a multilevel system, and Kumar et al.[26] have shown experimentally that such distortions affect cross-peak splittings. Further, the use of a noncollinear beam geometry causes detection distortions with no analogue in NMR.[22,23]

Belabas and Jonas[21,22] extended the monochromatic plane wave solutions of Maxwell's equations for wave mixing[27] to pulsed four-wave mixing (4WM) using finite beams in isotropic media with arbitrary optical density. Their solution is valid for an arbitrary nonlinear response under the approximation of "negligible nonlinear distortion" of the propagating beams.[22] Three types of distortions were found: absorptive/dispersive distortions, phase-mismatch distortions, and directional filtering distortions. Directional filtering arises from detection of a signal emerging in a noncollinear direction. Yetzbacher et al.[23] simulated these effects on peak shapes in 2D spectra recorded with the square BOXCARS geometry using the three-dimensional Fourier transform (3DFT) algorithm of ref 21 for Bloch,[28] Kubo,[29,30] and Brownian oscillator[31–33] relaxation models. Under typical weak signal/thin sample experimental conditions, the absorptive/dispersive and directional filtering distortions are experimentally significant for the 2D peak shapes, but phase-mismatch distortions are negligible. Yetzbacher et al.[23] found easily estimated dimensionless parameters that scale with each of the three distortions. This study extends the work of Yetzbacher et al.[23] to a multilevel Bloch model system and

† Part of the "Robert W. Field Festschrift".

* Corresponding author: david.jonas@colorado.edu; tel, (303) 492-3818; fax, (303) 492-5894.

‡ Current address: Kestrel Laboratories Inc., 3133 Indian Rd., Suite K, Boulder, CO 80301.

§ Current address: Digital Fusion Solutions, 5030 Bradford Dr., Huntsville, AL 35805.

10.1021/jp904504z CCC: $40.75
Published on Web 09/28/2009

examines the effect of propagation and detection distortions on noncollinear 2D spectra with cross peaks. NMR analogies led to early recognition that coherence makes femtosecond 2DFT spectra quite distinct from systematic double resonance and does not allow rigorous "frequency domain window" interpretations of finite pulse effects (or even absorptive/dispersive interpretations of real and imaginary 2D spectra) until after coherence has been destroyed.[5,6,34] For four-wave mixing, this makes exact frequency domain transformation to remove experimental distortions possible only in 3D.[22] Extending the work of Yetzbacher et al. on absorptive/dispersive distortions, a transformation of the 2D spectra is shown to eliminate directional filtering distortions after coherence is gone and found to match ideal 2D spectra more closely in the presence of coherence.

A complete description of calculations that include propagation and detection effects on 2DFT spectra is given by Yetzbacher et al.,[23] so the description is abbreviated here. Briefly, each excitation pulse is a linear superposition of plane waves that propagate linearly with optical electric field

$$\vec{E}(\vec{r}, t) = \frac{1}{2\pi}\int_{-\infty}^{\infty} \hat{E}(\omega)\exp[i(\hat{\mathbf{k}}\cdot\vec{\mathbf{r}} - \omega t)]\,d\omega \qquad (1)$$

where $\vec{\mathbf{r}}$ is position, t is time, $\hat{E}$ is the frequency domain electric field at the sample entrance, ω is the angular frequency, and $\hat{\mathbf{k}}$ is the complex-valued wave vector (the imaginary part incorporates attenuation in absorbing samples). The time-domain third-order nonlinear response tensor (from an analytic model in this paper) is numerically triple inverse Fourier transformed to yield the 3D frequency domain nonlinear susceptibility tensor, $\boldsymbol{\chi}^{(3)}$. For well-collimated beams and sufficiently thin samples, the distortions that multiply the susceptibility can be separated into a sample-dependent part (absorptive/dispersive and phase-mismatch distortion matrix, $\boldsymbol{\Pi}^{(3)}$) and purely beam geometry dependent part (directional filtering distortion function,$\Phi^{(3)}$)

$$S^{(3)} = [\boldsymbol{\Pi}^{(3)}(\boldsymbol{\chi}^{(3)}\vdots\hat{E}_a\hat{E}_b\hat{E}_c)]\cdot\hat{E}_d^{*}\Phi^{(3)} \qquad (2)$$

where $S^{(3)}$ is a distorted 3D frequency domain signal and $\hat{E}_{a,b,c,d}$ represent the excitation (a, b, c) and detection (d) pulse fields. The well-collimated beam assumption allows the frequency dependence of the central wave-vectors to convert $\boldsymbol{\Pi}^{(3)}$ into a function of beam geometry and the three excitation frequencies. For TE polarized beams and a sample with the same linear optical properties as the windows, the propagation matrix becomes a scalar

$$\Pi^{(3)}_{\text{exit}}(\hat{\mathbf{k}}^0_a, \hat{\mathbf{k}}^0_b, \hat{\mathbf{k}}^0_c, L) = \frac{\omega_t}{(\hat{\mathbf{k}}^0_s\cdot\mathbf{e}_z)c}\frac{\exp[i\Delta\hat{\mathbf{k}}^0\cdot\mathbf{e}_z L] - 1}{i\Delta\hat{\mathbf{k}}^0\cdot\mathbf{e}_z}\exp[i(\hat{\mathbf{k}}^0_s\cdot\mathbf{e}_z)L] \qquad (3)$$

where $\hat{\mathbf{k}}^0_a$, $\hat{\mathbf{k}}^0_b$, $\hat{\mathbf{k}}^0_c$, and $\hat{\mathbf{k}}^0_s$ are the complex-valued, frequency-dependent, central wave vectors of pulses a, b, c, and the signal, respectively; L is the sample length; ω_t is the frequency of the signal wave; c is the speed of light in vacuum; $\mathbf{e}_z$ is a unit vector normal to the plane parallel window−sample interfaces; and $\Delta\hat{\mathbf{k}}^0$ is the complex-valued 3D phase mismatch between the nonlinear polarization and signal waves. In this paper, eq 3 will be used as an approximation to $\Pi^{(3)}$ for a geometry in which one excitation pulse is TM polarized; this approximation becomes exact for normal incidence. This allows eq 2 to be interpreted as a scalar equation with a single susceptibility tensor element ($\chi^{(3)}_{XXXX}$ in this paper). Equation 3 shows that $\Pi^{(3)}_{\text{exit}}$ is a decreasing function with respect to the phase mismatch, which diminishes the observed nonlinear signal. In an absorbing sample (which is necessary for resonant signals), the complex-valued phase mismatch (the second factor) also implies excitation field attenuation.[22] The complex-valued signal wave vector in the last exponential reflects the signal attenuation when there is a sample absorption. Absorption, dispersion and phase mismatch are included in the 3D frequency domain propagation function $\Pi^{(3)}$. The calculation of $\Delta\hat{\mathbf{k}}^0$ (and therefore, $\Pi^{(3)}$) requires specification of the beam geometry.

In the rectangular BOXCARS geometry, the three excitation beams travel parallel to each other and occupy three corners of a rectangle on the lens that focuses them into the sample (see Figure 1 of ref 23). After the sample, the signal occupies the fourth corner of the rectangle on the collimating lens and obeys the phase matching condition

$$\hat{\mathbf{k}}^0_s(\omega_t)\cdot\mathbf{e}_{x,y} = [\hat{\mathbf{k}}^0_a(-\omega_a) + \hat{\mathbf{k}}^0_b(\omega_b) + \hat{\mathbf{k}}^0_c(\omega_c)]\cdot\mathbf{e}_{x,y} \qquad (4)$$

with

$$\hat{\mathbf{k}}^0(\omega)\cdot\hat{\mathbf{k}}^0(\omega) = (\omega^2/c^2)\hat{n}^2(\omega) \qquad (5)$$

for all four beams (a, b, c, s). In eqs 4 and 5, $\hat{n}$ is the complex refractive index of the sample. (The simplification $\mathbf{k}_s \approx -\mathbf{k}_a + \mathbf{k}_b + \mathbf{k}_c$ only works in transparent samples. On the basis of eq 1, for positive ω_b, Re[$\hat{\mathbf{k}}^0_b(\omega_b)$] points along the propagation direction of beam b; the direction of propagation is given by the relative signs of Re[$\hat{\mathbf{k}}(\omega)$] and ω. Both Re [$-\hat{\mathbf{k}}^0_a(\omega_a)$] and Re[$\hat{\mathbf{k}}^0_a(-\omega_a)$] point opposite the propagation direction of beam a. However, for complex-valued wavevectors $\hat{\mathbf{k}}(\omega) = -\hat{\mathbf{k}}^*(-\omega)$, so the two differ in that for $\hat{\mathbf{k}}^0_a(-\omega_a)$, beam a is correctly attenuated as it propagates toward the back of the sample while $-\hat{\mathbf{k}}^0_a(\omega_a)$ would incorrectly amplify the beam.)

The propagation-distorted 3D frequency domain signal is further distorted through multiplication by the directional filter, $\Phi^{(3)}$, which is dictated by beam crossing geometry and beam size. For a rectangular beam crossing geometry and Gaussian beams with frequency independent waist, w_0

$$\Phi^{(3)}(\omega_a - \omega_b - \omega_c) = \exp[-(\omega_a - \omega_b)^2 w_0^2 \sin^2(\theta)/2c^2] \times \exp[-(\omega_a - \omega_c)^2 w_0^2 \sin^2(\phi)/2c^2] \qquad (6)$$

where ω_a, ω_b, and ω_c are the frequencies of pulses a, b, and c, respectively, and 2θ (2ϕ) is the external crossing angle between beams a and c (a and b). Equation 6 assumes that parallel beams are brought to a common focus by a single lens or mirror (as in refs 5 and 15) and does not apply to experiments with diffractive optics (as in refs 16, 35, and 36). In the spectrally resolved pump−probe geometry, $\phi = 0$ so that $\Phi^{(3)} = \exp[-(\omega_a - \omega_b)^2 w_0^2 \sin^2(\theta)/2c^2]$.[23]

After multiplication by $\boldsymbol{\Pi}^{(3)}$ and $\Phi^{(3)}$, the distorted 3D susceptibilty is then multiplied by the three frequency domain excitation fields and the interference detection field to generate a 3D frequency domain signal. This 3D frequency domain signal is triple Fourier transformed back to the 3D time domain, yielding the distorted time domain signal. At this stage, the signal is a three-dimensional object, dependent on three time

variables. From the 3D time domain signal, we extract the signal corresponding to the scan procedure used in the 4WM experiment, which is a function of τ and t at a fixed T (see ref 37). In 2D correlation and relaxation spectroscopy, τ is the time interval between the first two pulses (a and b, which can arrive in either order), T is the interval between the second pulse (b or a) and the third pulse (c), and t is the running time after pulse (c), as a function of which the signal field is measured. Inverse Fourier transforming with respect to the two experimentally controlled time dimensions, τ and t, finally yields the 2D spectrum. The interference detection field must be specified in order to represent the 2D spectrum. In this study, the experimentally accessible FID-referenced representation of the 2D spectrum, $\hat{S}^0_{2D}$, will be used exclusively as a starting point for transforming to other representations. $\hat{S}^0_{2D}$ corrects for dispersive distortion of the signal and is the most commonly used representation of the experimental 2D spectrum.[5,23]

Transformations of $\hat{S}^0_{2D}$ will be performed according to eq 25 in ref 23. The representation

$$\hat{S}^{++}_{2D}(\omega_t,\omega_\tau;T) = \frac{2\mathrm{Im}(\hat{\mathbf{k}}_a(\omega_\tau)\cdot\mathbf{e}_z)L}{1-\exp[-2\mathrm{Im}(\hat{\mathbf{k}}_a(\omega_\tau)\cdot\mathbf{e}_z)L]}\times \exp[+\mathrm{Im}(\hat{\mathbf{k}}_d(\omega_t)\cdot\mathbf{e}_z)L]\hat{S}^0_{2D}(\omega_t,\omega_\tau;T) \quad (7)$$

corrects for absorption of the excitation beams and signal in the limit when all coherence has decayed. We define an additional transformation of the measured 2D spectrum:

$$\hat{S}^{FX}_{2D}(\omega_t,\omega_\tau;T) = \frac{\hat{S}^X_{2D}(\omega_t,\omega_\tau;T)}{\exp[-(\omega_\tau-\omega_t)^2 w_0^2 \sin^2(\phi)/2c^2]} \quad (8)$$

The denominator in eq 8 is simply the approximate directional filter of eq 6 in the limit $\omega_a = \omega_b = \omega_\tau$. The transformation described by eq 8 can be performed on any representation of the 2D spectrum (here $\hat{S}^0_{2D}$ or $\hat{S}^{++}_{2D}$ are used to generate $\hat{S}^F_{2D}$ and $\hat{S}^{F++}_{2D}$, respectively) and will undo the effects of the directional filter to the extent that the first two fields generating the signal have equal frequencies. In the absence of phase-matching distortions, $\hat{S}^{F++}_{2D}$ becomes identical to the ideal 2D spectrum when T is long enough to decorrelate the absorption and emission frequencies both within and between dynamically broadened 2D peaks.

II. The Four-Level Model System

The nonlinear response for the multilevel system is obtained by the methods given in refs 20, 38, and 39. The energy level scheme for the system is shown in Figure 1. ω_{eg} is the average transition frequency from the ground state (0) to the singly excited states (α and β), which are split by Δ. The average transition frequency from the two singly excited states to the doubly excited state (2) is $\omega_{eg}-d$. The red shift of the doubly excited state could result from a cross anharmonicity (in vibrational spectroscopy[11]) or a biexciton shift (in electronic spectroscopy[40]). The transitions to the singly excited states have frequencies $\omega_{\alpha 0}$ and $\omega_{\beta 0}$. These two transitions have equal magnitude, perpendicular transition dipole moments, $\mu\hat{y}$ and $\mu\hat{x}$, respectively, in the molecular frame. The transitions to the doubly excited state have frequencies $\omega_{2\alpha}$ and $\omega_{2\beta}$, indicating their origin from the levels α and β, respectively. The transition at $\omega_{2\alpha}$ has the transition dipole moment $\mu\hat{x}$ and transition at $\omega_{2\beta}$ has transition dipole moment $\mu\hat{y}$. This level scheme is

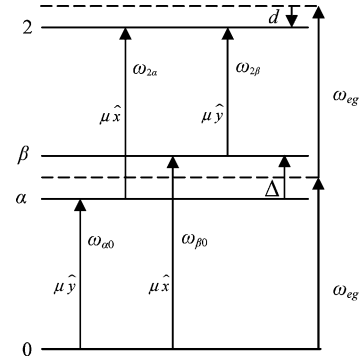

Figure 1. The model four-level system for calculated 2D spectra. ω_{eg} is the average transition frequency from the ground state (0) to the singly excited states (α and β) which have the splitting Δ. The average transition frequency from the singly excited states to the doubly excited state (2) is $\omega_{eg}-d$. d is the average red shift from ω_{eg} of excited state absorption to the doubly excited state. $\omega_{\alpha 0}$ and $\omega_{\beta 0}$ denote the transition frequencies from the ground to the singly excited states, α and β, respectively. $\omega_{2\alpha}$ and $\omega_{2\beta}$ denote the transition frequencies from the singly excited states α and β to the doubly excited state. $\mu\hat{x}$ and $\mu\hat{y}$ indicate the equal magnitude, perpendicular transition dipole moments.

appropriate for two perpendicular chromophores in either electronic or vibrational spectroscopy. The application to vibrational spectroscopy requires that the "vibrational overtone levels" ($v_\alpha = 2$, $v_\beta = 0$) and ($v_\alpha = 0$, $v_\beta = 2$) have smaller anharmonic shifts than the "combination level" ($v_\alpha = 1$, $v_\beta = 1$) and that the transitions be well-resolved—both are often the case for localized vibrations.[41,42]

The four-wave mixing signals that result from the interaction of the fields with the model system can be calculated within the framework of density matrix perturbation theory.[19,43,44] The fields induce a nonlinear polarization that acts as the source for the radiated signal. In the impulsive limit, the nonlinear polarization is proportional to the nonlinear response function. Typically, the inverse line width of a vibrational transition in a room temperature liquid (~1 ps) is much slower than fluctuations in liquid structure (~100 fs), so the frequency−frequency correlation function can be approximated as decaying instantaneously, making the Bloch model (exponential decay of coherence) useful for vibrational spectroscopy. We assume coherence dephasing rates $\Gamma_{\alpha 0} = \Gamma_{\beta 0} = \Gamma_{2\alpha} = \Gamma_{2\beta} = \gamma_{\mathrm{optical}}$, and $\Gamma_{\alpha\beta} = \gamma_{\mathrm{qb}}$, where Γ_{ij} indicates the dephasing rate for coherence between levels i and j, $\gamma_{\mathrm{optical}}$ is a common dephasing rate for all optical transitions, and γ_{qb} is the dephasing rate for the quantum beats between singly excited levels. The parameters in this study are chosen to model carbonyl stretching vibrations,[15,45] but coherence transfer relaxation processes are neglected for simplicity.

The coherence pathways that give rise to the 4WM signal in the square BOXCARS beam geometry are summarized in Table 1. The rotating wave approximation is implicitly applied; coherence pathways that do not satisfy the resonance condition are omitted. Further, only pathways contributing to the 2D spectrum with positive ω_t are included. Following the notation used in ref 10, the pathways contributing to the 4WM signal are classified as ground state bleach (GSB: D3 and D4), excited state emission (ESE: D1 and D2), excited state absorption (ESA: D5 and D6), and double quantum coherence (DQC: D7 and D8). We neglect DQC pathways (not shown in Table 1) because they only contribute to 2D correlation and relaxation spectra when all three pulses overlap. In each remaining category, one diagram represents an "N-type" coherence pathway (D2, D3,

TABLE 1: Coherence Pathways That Contribute to 2D Relaxation Spectra in the Square BOXCARS Beam Geometry

Excited State Emission									
b a c (−τ)					*a b c* (+τ)				
D_1	$1d_1$	$1d_2$	$1d_3$	$1d_4$	D_2	$2d_1$	$2d_2$	$2d_3$	$2d_4$
t	α0	*β*0	*β*0	α0	*t*	α0	*β*0	α0	*β*0
T	αα	*ββ*	*β*α	α*β*	*T*	αα	*ββ*	α*β*	*β*α
τ	α0	*β*0	*β*0	α0	τ	0α	0*β*	0*β*	0α
Ground State Bleach									
b a c (−τ)					*a b c* (+τ)				
D_4	$4d_1$	$4d_2$	$4d_3$	$4d_4$	D_3	$3d_1$	$3d_2$	$3d_3$	$3d_4$
t	α0	*β*0	α0	*β*0	*t*	α0	*β*0	α0	*β*0
T	00	00	00	00	*T*	00	00	00	00
τ	α0	*β*0	*β*0	α0	τ	0α	0*β*	0*β*	0α
Excited State Absorption									
b a c (−τ)					*a b c* (+τ)				
D_6	$6d_1$	$6d_2$	$6d_3$	$6d_4$	D_5	$5d_1$	$5d_2$	$5d_3$	$5d_4$
t	2α	2*β*	2α	2*β*	*t*	2α	2*β*	2*β*	2α
T	αα	*ββ*	*β*α	α*β*	*T*	αα	*ββ*	α*β*	*β*α
τ	α0	*β*0	*β*0	α0	τ	0α	0*β*	0*β*	0α

The pathways are classified into four groups: ground state bleach (GSB: D_3 and D_4), excited state emission (ESE: D_1 and D_2), excited state absorption (ESA: D_5 and D_6). Each diagram, D_N, further divides into four subdiagrams, Nd_1, Nd_2, Nd_3, and Nd_4 (see text for detail). τ is the time interval between the first and the second pulse and is positive if the pulse *a* arrives before the pulse *b*. *T* is the time interval between the second and third pulse. *t* is the time interval between the third pulse and the detection of the signal. The left half of the table represents P-type coherence pathways corresponding to the pulse order *b*−*a*−*c* (τ < 0) and the right half of the table represents N-type coherence pathways corresponding to the pulse order *a*−*b*−*c* (τ > 0). Coherence evolution during each time interval is specified by the entries in the table. For example, the *β*0 entry for $6d_3$ during τ, specifies coherence between states *β* and 0. The relative order *β*0 during τ and 2α during *t* for $6d_3$ is significant, specifying a P-type pathway because the higher energy state is first during both τ and *t*. The entries for subdiagram $6d_3$ show *β*0, *β*α and 2α coherence during τ, *T* and *t*, respectively; the complex conjugate contribution for every pathway [e.g. (0*β*, α*β*, α2) for $6d_3$] contributes to a symmetry related quadrant of the 2D spectrum (not shown) in which both ω_τ and ω_t have opposite signs.

D5), corresponding to the pulse order *a*−*b*−*c*, and one diagram represents a "P-type" coherence pathway (D1, D4, D6), corresponding to the pulse order *b*−*a*−*c*.[2,46] The designations "P" (positive) and "N" (negative) refer to the relative sign of the phase evolution for the term of the density matrix represented by each diagram in the first (τ) and the third (*t*) periods. In a two-level system, N-type coherence pathways can lead to inhomogeneous rephasing (and the formation of echoes) whereas P-type coherence pathways cannot.

Each diagram further divides into four subdiagrams: subdiagrams d_1 and d_2 represent coherence pathways that only involve α or *β*, respectively, and no other singly excited levels at all times.[39] Subdiagrams d_3 and d_4 represent coherence pathways that involve *β* or α, respectively, in the first time interval, and involve the other singly excited level at a later time.[39] In a multilevel system, anticorrelated inhomogeneities can rephase for P-type coherence pathways. This has led to the N-type ("echo") vs P-type ("anti-echo") labeling used in NMR.[2] In the model system, symmetric (asymmetric) vibrations that are coupled to the energy levels can cause correlated (anticorrelated) inhomogeneity. For example, the P-type ground state bleaching subdiagram $4d_4$ would rephase an anticorrelated inhomogeneity in the level splitting to produce an echo. Such anticorrelated splitting could be caused by inhomogeneity in the off-diagonal coupling between two chromophores. Under such circumstances, the corresponding N-type subdiagram, $3d_4$, would not produce rephasing. For these reasons, the common nonlinear optical labeling of N-type pathways as "rephasing" and P-type pathways as "non-rephasing" is not used in this paper. For the level scheme in Figure 1, the homogeneously broadened model system parameters chosen here prevent all inhomogeneous rephasing.

The contribution of each subdiagram to the response can be written as a product of Green functions which describe the time evolution of each density matrix element following a sudden excitation.[19] For example, the response function, R^{6d_3}, is given by

$$R^{6d_3}(t_1,t_2,t_3) = -(i/\hbar)^3\langle(\vec{\mu}_{\alpha 2}\cdot\vec{E}_d)(\vec{\mu}_{2\beta}\cdot\vec{E}_c)\times (\vec{\mu}_{0\alpha}\cdot\vec{E}_a)(\vec{\mu}_{\beta 0}\cdot\vec{E}_b)\rangle_{\text{orientational}}\langle G_{2\alpha}(t_3)G_{\beta\alpha}(t_2)G_{\beta 0}(t_1)\rho_{00}\rangle_{\text{ensemble}} \quad (9)$$

where the first factor, $-(i/\hbar)^3$, is the absorption/emission factor, the second is the orientational average factor, and the third is the product of Green functions. The second factor is geometrical and contains a cyclic set of transition dipoles, each dotted into an external field; the brackets indicate an orientational average over an isotropic distribution of static molecular orientations. The third factor contains all the time-dependent dynamics in the Green functions; the brackets indicate the average over an ensemble. If the Hamiltonian is invariant under time reversal, the geometrical factor is real since the eigenfunctions may be taken to be real and orthogonal.[37,47] The sets of transition dipoles can be rearranged to the cyclic form $\langle a|\mu|b\rangle\langle b|\mu|c\rangle\langle c|\mu|d\rangle\langle d|\mu|a\rangle$, showing that the physically significant overall sign of the cyclic set is independent of the arbitrary wave function phases.[37] If two of the four levels involve symmetry-required degeneracy, the sign of the transition dipole product is dictated by the symmetry of the four levels. Otherwise, the sign depends on the particular levels involved.[48] The transition moments in Figure 1 are those for uncoupled oscillators;[48] the transition dipoles connecting each singly excited state to the ground and doubly excited states are orthogonal. In this paper, the geometrical factors are calculated for an all parallel polarization geometry (e.g., all optical electric fields have X polarization in the lab frame).[48,49]

In the Bloch limit, $G_{jk}(t) = \theta(t)\exp(-\Gamma_{jk}t)\exp(-i\omega_{jk}t)$ where $\theta(t)$ is the Heaviside step function, ω_{jk} is the Bohr frequency $(E_j - E_k)/\hbar$, and Γ_{jk} is the relaxation rate.[19] The ensemble averaged product of Green functions for subdiagram $6d_3$ is given by

$$\langle G_{\beta 0}(t_1)G_{\beta\alpha}(t_2)G_{2\alpha}(t_3)\rangle = \theta(t_1)\exp[-i\omega_{\beta 0}t_1]\times \exp[-\Gamma_{\beta 0}t_1]\theta(t_2)\exp[-i\omega_{\beta\alpha}t_2]\exp[-\Gamma_{\beta\alpha}t_2]\theta(t_3)\times \exp[-i\omega_{2\alpha}t_3]\exp[-\Gamma_{2\alpha}t_3] \quad (10)$$

For pulse ordering *b*−*a*−*c*, using the definitions in ref 37, $t_1 = -\tau$, $t_2 = T$, and $t_3 = t$ for delta function pulses; $\theta(t_1)$ is zero for positive τ, and $\theta(t_3)$ zero for negative *t*. In the absence of distortions, the inverse Fourier transform of eq 10 with respect to τ and *t* yields a peak in the 2D spectrum at a fixed *T*

$$\hat{S}_{6d_3}(\omega_\tau, \omega_t; T) = F^{-1}[G_{\beta 0}(\tau)]G_{\beta\alpha}(T)F^{-1}[G_{2\alpha}(t)] = [a_{\beta 0}(-\omega_\tau) - id_{\beta 0}(-\omega_\tau)]\exp[-i\omega_{\beta\alpha}T] \times \exp[-\Gamma_{\beta\alpha}T][a_{2\alpha}(\omega_t) - id_{2\alpha}(\omega_t)] \quad (11)$$

where $a_{ij}(\omega) = \Gamma_{ij}/[\Gamma_{ij}^2 + (\omega_{ij} - \omega)^2]$ is the absorptive Lorentzian line shape and $d_{ij}(\omega) = (\omega_{ij} - \omega)/[\Gamma_{ij}^2 + (\omega_{ij} - \omega)^2]$ is the dispersive Lorentzian line shape (in the rotating wave approximation). The total response function for diagram D_6 is the sum of the responses for all four of its subdiagrams: $R^{D6} = R^{6d_1} + R^{6d_2} + R^{6d_3} + R^{6d_4}$. Since the 2D FT is linear, the 2D spectra from the various subdiagrams can be added to generate the overall 2D spectra. Nonlinear signals generated from the coherence pathways shown in Table 1 can be inverse Fourier transformed and summed to produce the ideal 2D spectrum.

Figure 2 shows a schematic 2D spectrum expected from the model system. $DP_{\alpha\alpha 0}$ and $DP_{\beta\beta 0}$ denote the diagonal peaks resulting from the excitation frequency being equal to the radiated signal frequency. $DP_{\alpha\alpha 2}$ and $DP_{\beta\beta 2}$ indicate the "diagonal" peaks that result from the transitions involving the red-shifted doubly excited state. The red shift causes them to appear to the red of the diagonal in ω_t. $CP_{\alpha\beta 0}$ and $CP_{\beta\alpha 0}$ denote the cross peaks arising from transitions only involving the ground and singly excited states. $CP_{\alpha\beta 2}$ and $CP_{\beta\alpha 2}$ indicate cross peaks that result from transitions involving the doubly excited state. Figure 2 shows how each subdiagram contributes to each observed peak. For example, subdiagrams $1d_1$, $2d_1$, $4d_1$, $3d_1$, and $1d_4$ sum to generate $DP_{\alpha\alpha 0}$. For every peak, the associated subdiagrams are separated into two columns; the left side has the pulse order $b-a-c$ (P-type, "antiecho", $-\tau$) and the right, $a-b-c$ (N-type, "echo", $+\tau$). Experimentally, signals from the negative τ scan are added to those of the positive τ scan (either by a continuous scan of τ,[3] spliced scans of τ in the time domain[5] or addition of 2D spectra in the frequency domain,[12]). This scanning procedure corresponds to summing signal contributions from the subdiagrams of the left and right columns, in order to bring a balance between the N- and P-type diagrams, where possible.

The procedure to balance N- and P-type coherence has its origin in NMR spectroscopy;[2] in 2D correlation or relaxation spectra, it is useful to generate purely absorptive line shapes in the real part of the spectra because they allow extraction of information from the line shape and width, and it is well-known that an absorptive line shape is obtained when signals from N-type and, P-type scans are added with equal weights.[2] When N- and P-type scans are balanced, the dispersive line shapes from individual subdiagrams cancel in the real 2D spectra because they carry opposite signs.[2] For a two-level system, the above-mentioned scanning procedure reflects the symmetry with respect to interchange of the first and second pulses at nonzero T and ensures the balance of the N- and P-type diagrams. Hybl et al.[3,5] and Khalil et al.[12] demonstrated in 2D electronic and 2D-IR measurements, respectively, that absorptive real peaks can be generated by the above scanning methods. However, as depicted in Figure 2, the model system generates 2D peaks that contain unpaired subdiagrams, thus setting up an inherent imbalance of N- and P-type coherence; the resulting lineshapes are "phase-twisted".[12] As noted by Hybl et al.[3,5,6] and Khalil et al.,[11,12,15] the balance is not achieved as long as the unpaired subdiagrams survive or are unequally weighted by intrinsic properties (e.g., echoes, polarization dependence). The combination of energy level splitting (Δ) and the red shift of the doubly excited state (d) gives rise to unpaired subdiagrams. When $\Delta = 0$, the eight peaks in Figure 2 collapse into two: $DP_{\alpha\alpha 0}$, $DP_{\beta\beta 0}$, $CP_{\alpha\beta 0}$ and $CP_{\beta\alpha 0}$ merge into a single positive peak at ω_{eg}; $DP_{\alpha\alpha 2}$, $DP_{\beta\beta 2}$, $CP_{\alpha\beta 2}$, and $CP_{\beta\alpha 2}$ merge into a single negative peak at $\omega_{eg} - d$. Both peaks are N/P balanced. When $d = 0$, the eight peaks collapse into four: $DP_{\alpha\alpha 2}$ merges into $DP_{\alpha\alpha 0}$ and $DP_{\beta\beta 2}$ into $DP_{\beta\beta 0}$; $CP_{\alpha\beta 2}$ merges into $CP_{\alpha\beta 0}$ and $CP_{\beta\alpha 2}$ into $CP_{\beta\alpha 0}$. If the sample's relaxation times are unaltered by excitation, the cross peaks and unpaired subdiagrams can cancel to leave two N/P balanced positive peaks split by Δ. The oscillatory contribution for each unpaired subdiagram decays with the factor $\exp[-\Gamma_{\alpha\beta}T]$: for $T \gg 1/\Gamma_{\alpha\beta}$ the contribution of the unpaired subdiagrams is negligible. The above discussion does not include DQC (interaction orders $b-c-a$ and $c-b-a$) or the "improperly ordered" diagrams (interaction order $c-a-b$), which contribute only when pulse c overlaps pulse a or b. These diagrams can break N/P balance when they contribute to the signal.[6]

The contribution of the each subdiagram to the overall peak shape/amplitude is weighted by the orientational factor, leading to a varying degree of time dependence of the peak shapes in the interval where $\exp[-\Gamma_{\alpha\beta}T] > 0$. For example, a single subdiagram $6d_3$ ($6d_4$) represents $DP_{\beta\beta 2}$ ($DP_{\alpha\alpha 2}$); for those two peaks, the entire peak amplitude undergoes modulation as a

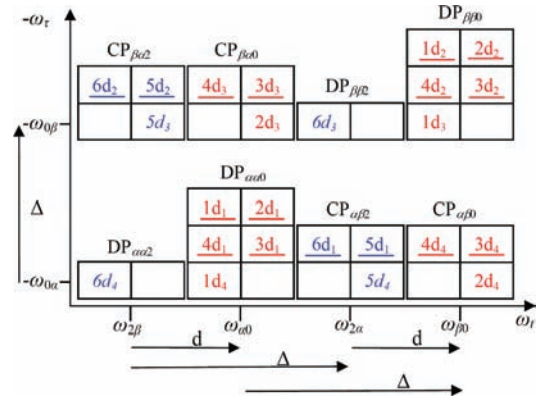

Figure 2. The schematic representation of the 2D spectrum generated from the model four-level system. The vertical and horizontal axes represent the excitation (ω_τ) and the detection (ω_t) frequencies, respectively. Δ and d are the energy level splitting, and the red shift of the doubly excited state, respectively, in Figure. 1. Diagonal peaks are denoted by $DP_{\alpha\alpha 0}$, $DP_{\beta\beta 0}$, $DP_{\alpha\alpha 2}$, and $DP_{\beta\beta 2}$. Cross peaks are denoted by $CP_{\alpha\beta 0}$, $CP_{\beta\alpha 0}$, $CP_{\beta\alpha 2}$, and $CP_{\alpha\beta 2}$. The subscripts indicate the positions of peaks in the 2D spectrum; the subscript $ii0$ or $ii2$, where $i = \alpha(\beta)$, indicates a diagonal peak stemming from an $\omega_{\alpha 0}(\omega_{\beta 0})$ excitation; $ij0$ or $ij2$, where $i \neq j = \alpha(\beta)$, indicates a cross peak stemming from an $\omega_{\alpha 0}(\omega_{\beta 0})$ excitation; for the last subscript, 0 indicates GSB or ESE detection pathways and 2 indicates ESA detection pathways. Each peak results from the sum of contributions from the coherence pathways denoted by the subdiagrams which are separated into two columns; the left column contains subdiagrams representing coherence pathways involving the pulse order $b-a-c$ for negative τ (P-type, "antiecho"); the right column contains the subdiagrams representing coherence pathways involving the pulse order $a-b-c$ for positive τ (N-type, "echo"). (In a two-level system, N-type subdiagrams cause inhomogeneous rephasing and P-type diagrams are nonrephasing; the "rephasing" vs "non-rephasing" classification is not generally meaningful for multilevel systems.) Paired subdiagrams indicate a smooth transition from the $b-a-c$ pulse order (negative τ) to $a-b-c$ pulse order (positive τ), and the balance of N-, P-type coherence. The unpaired subdiagrams break the balance and are a result of the split singly excited states and the red shift of the doubly excited state (see text). The subdiagrams in red ($DP_{\alpha\alpha 0}$, $DP_{\beta\beta 0}$, $CP_{\alpha\beta 0}$, and $CP_{\beta\alpha 0}$) have positive real peak amplitudes and the subdiagrams in blue ($DP_{\alpha\alpha 2}$, $DP_{\beta\beta 2}$, $CP_{\beta\alpha 2}$, and $CP_{\alpha\beta 2}$) have negative real peak amplitudes. Italics indicate subdiagrams whose sign may be indeterminate due to a cyclic transition dipole product (see text, the sign is fixed by the choice of model system). The underlined subdiagrams do not evolve through $\alpha\beta$ coherence during T and hence do not oscillate with T.

function of T. Because the peak is pure P-type, it will have the fully phase-twisted shape shown in Figure 6.5.1(f) of ref 2. On the other hand, the subdiagram $1d_4$ in $DP_{\alpha\alpha0}$ contributes only 1/13 of the overall peak amplitude (orientational factors for $1d_1$, $2d_1$, $3d_1$, and $4d_1$ are each 1/5 compared to 1/15 for $1d_4$) so it is 1/13 phase-twisted, as is $DP_{\beta\beta0}$. These two peaks are nearly N/P balanced, have a small phase-twist, and have weak quantum beat modulation. The subdiagrams $2d_3$, $2d_4$, $5d_3$, and $5d_4$ in $CP_{\beta\alpha0}$, $CP_{\alpha\beta0}$, $CP_{\beta\alpha2}$, and $CP_{\alpha\beta2}$, respectively, each contribute 1/3 (all subdiagrams have orientational factors of 1/15) of the total amplitude for their cross peaks. The modulation for these peaks is correspondingly weaker compared to the fully modulated peaks, $DP_{\alpha\alpha2}$ and $DP_{\beta\beta2}$. The partially (1/3) phase-twisted shape of the cross peaks is shown in Figure 4 of ref 6.

The analytical model for the nonlinear response uses the nonlinear response functions of a dimer.[39] The internal motions that cause the transition energies to fluctuate in a dimer can be separated into symmetric and asymmetric vibrations. The dephasing caused by symmetric and asymmetric vibrations are thus represented by symmetric and asymmetric line shape functions, which are specified by symmetric and asymmetric dephasing rates in the optical Bloch limit. The line shape functions to use in eqs 3 and 4 of ref 39 for the calculation of the nonlinear response are therefore

$$g_s(t) = \gamma_s t \tag{12a}$$

$$g_{as}(t) = \gamma_{as} t \tag{12b}$$

where γ_s indicates symmetric dephasing and γ_{as} asymmetric dephasing. The Green functions in eq 9 can be broken down into complex exponentials that describe the evolution of coherences and population decay, and dephasing functions that reflect the symmetric ($F_s nd_i$) and asymmetric ($F_{as}^{nd_i}$) vibrational motions. As a result, the Green function for R^{6d3} can be written as

$$\begin{aligned}\langle G_{\beta0}(t_1)G_{\beta\alpha}(t_2)G_{2\alpha}(t_3)\rangle &= \exp[-i\omega_{\beta0}t_1 - i\omega_{\beta\alpha}t_2 - i\omega_{2\alpha}t_3]F_s^{D6}F_{as}^{6d3} \\ &= \exp[-i\omega_{eg}t_1 - i(\omega_{eg} - d)t_3] \times \exp[-i(\Delta t_1 + 2\Delta t_2 + \Delta t_3)/2] \times \exp[-\gamma_{optical}(t_1 + t_3) - \gamma_{qb}t_2]\end{aligned} \tag{13}$$

where $F_s^{D6} = \exp[-\gamma_s(t_1 + t_3)]$ is obtained by substituting eq 12a into eq 3 of ref 39 and $F_{as}^{6d3} = \exp[-\gamma_{as}(t_1 + 4t_2 + t_3)]$, by substituting eq 12b into eq 4 of ref 39, so that $F_s^{D6}F_{as}^{6d3}$ equals the last exponential in the second equality with dephasing rates, $\gamma_{optical} = \gamma_s + \gamma_{as}$ and $\gamma_{qb} = 4\gamma_{as}$. The complex exponentials of the second equality in eq 13 are deduced by noting $\omega_{2\alpha} = \omega_{eg} + \Delta/2 - d$, $\omega_{\beta0} = \omega_{eg} + \Delta/2$, and $\omega_{\beta\alpha} = \Delta$. When $\Delta = 0$, $R^{Nd1} = R^{Nd2}$ and $R^{Nd3} = R^{Nd4}$, so the sums, $R^{Nd1} + R^{Nd2}$ and $R^{Nd3} + R^{Nd4}$, can be written as products of the $\Delta = 0$ response and a function of Δ.

$$\begin{aligned}&R^{6d3}(t_1, t_2, t_3) + R^{6d4}(t_1, t_2, t_3) \\ &= R^{6d3}_{unsplit}(t_1, t_2, t_3)2\cos[(\Delta t_1 + 2\Delta t_2 + \Delta t_3)/2] \\ &= R^{6d3}_{unsplit}(\tau, T, t)2\cos[(\Delta\tau + 2\Delta T + \Delta t)/2]\end{aligned} \tag{14}$$

where $R^{6d3}_{unsplit}$ is the response function in the absence of the splitting ($\Delta = 0$ in eq 13). Similar expressions can be derived for the remaining subdiagrams. Equation 14 shows how the splitting shifts the excitation and detection frequencies relative to ω_{eg} and causes the signal field to oscillate as a function of T. 2D inverse Fourier transformation of the response in eq 14 with respect to the first and third time intervals thus gives rise to the peaks $DP_{\alpha\alpha2}$ and $DP_{\beta\beta2}$. The oscillation during T is due to the coherence between the α and β levels and decays at quantum beat coherence dephasing rate $\Gamma_{\alpha\beta}$. As a function of T, all peaks in the 2D spectrum will oscillate at the frequency Δ until the decay of the quantum beats is complete.

III. Simulation of Beam Propagation/Geometry Effect on 2D Spectra

The simulation is carried out for an ideal case, $\alpha_{max}L = 0$ ($\Pi^{(3)} = 1$) and for $\alpha_{max}L = 0.25$ and 0.5 ($OD_{max} = 2\alpha_{max}L/\ln(10)$); the corresponding optical densities are ~0.22 and 0.43, respectively) for a sample length of 200 μm. We apply the rotating wave approximation; the average transition frequency, $\omega_{eg}/2\pi c = 2049.5\ cm^{-1}$, is demodulated by subtracting ω_{eg} from all single excitation transition frequencies (setting $\omega_{eg} = 0$ in eq 13) in the response, and adding ω_{eg} to ω_t, and subtracting ω_{eg} from ω_τ in $\Pi^{(3)}$, $\Phi^{(3)}$, and the axes for the 2D spectra. The excitation beams are modeled as delta function pulses that cross in the sample with half angles, $\theta = \phi = 5°$ and beam waist, $w_0 = 150\ \mu$m at the focus. The waist and crossing angles are larger than those in the 2D electronic simulation of ref 23 in order to reflect common beam parameters in the IR. The symmetric and asymmetric dephasing times, $1/\gamma_s$ and $1/\gamma_{as}$ are both set to 8.16 ps. The excited state lifetime is set to 1 ns. The splitting is $\Delta/2\pi c \approx 69.8\ cm^{-1}$; the red shift is $d/2\pi c \approx 26.8\ cm^{-1}$.

Calculations were done with FORTRAN95 code on a 2 GHz, Pentium 4 computer with 2 GB of RAM, which allows up to $486 \times 486 \times 486$ (486^3) grid for double precision calculations. The time step in the 3DFT is 118 fs (this is exactly a quarter period of quantum beat oscillation due to the splitting—the splitting and red shift are chosen to make sure that the maxima of the peaks fall on grid points). Convergence was checked by comparing the 2D spectra and time domain signals with different numbers of points in the 3D grid. When the frequency domain resolution is held constant, the largest magnitude differences in the 2D signals between a 256^3 grid and 486^3 grid are ~3% over the plotted region. A similar comparison of the time domain signals with the time increment held constant shows that the time domain 2D signals differ by ~3%. This level of convergence is slightly worse than the 2% reported in ref 23. The accuracy of the calculated 2D spectra on the 486^3 grid was checked against the analytic expression for ideal Bloch model spectra (generated by a sum of 2D spectra for individual diagrams such as in eq 11). The maximum convergence error of ~1% between calculated and analytic 2D spectra occurs in the extreme wings of the imaginary 2D spectra. A bigger convergence error compared to the two-level study of Yetzbacher et al.[23] (which yielded ~0.3%) is expected because the multilevel system produces peaks that are closer to the edge of the grid. Convergence errors increase with optical density and are estimated at 2% for the 2D spectra with $\alpha_{max}L = 0.5$.

IV. Results

1. Ideal Multilevel 2D Spectra. Before showing the distorted 2D spectra, we briefly discuss the undistorted 2D spectra and the associated spectrally resolved pump−probe signal. Figure 3 shows the time evolution of the undistorted spectrum (S_{2D}^{Ideal}) as a function of T. From the top to bottom, the spectra are shown at T = 118, 236, 354, 472 fs, i.e., every quarter period of quantum beat. The peak shapes and amplitudes vary periodically as a function of T, with frequency Δ. As anticipated from Figure

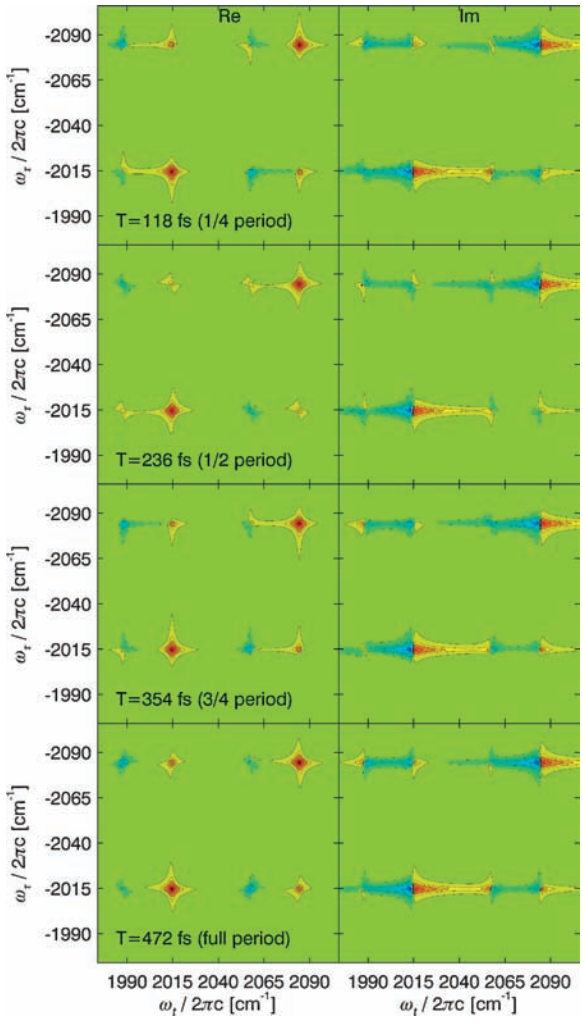

Figure 3. Undistorted four-level 2D spectra ($\hat{S}_{2D}^{Ideal}$) in the Bloch dephasing limit shown as a function of the mixing time, T. Displayed are the calculated real (left column) and imaginary (right column) part of the spectra. From the top to bottom, the spectra are shown at 118, 236, 354, 472 fs ($2\pi n/(4\Delta)$ where Δ is the frequency splitting in Figure 1 and $n = 1-4$). Grid time step = 118 fs; symmetric and asymmetric dephasing time, $1/\gamma_s$ and $1/\gamma_{as} = 8.16$ ps; demodulation frequency, $\omega_{eg}/2\pi c = 2049.5$ cm^{-1}; frequency splitting between singly excited states, $\Delta/2\pi c = 69.8$ cm^{-1}; red shift of the doubly excited state, $d/2\pi c = 26.8$ cm^{-1}. Contour levels are −90, −80, −70, −60, −50, −40, −30, −20, −10, −7, −4, 1, 1, 4, 7, 10, 20, 40, 60, 80, 90% with dotted contours indicating negative amplitude.

2, the cross peaks and ESA peaks show a stronger dependence on T, whereas the diagonal peaks display a weak dependence on T. All peaks in the real part of the spectra deviated from the well-known 2D Lorentzian star-shape indicative of exponential coherence decay; the real peaks are all phase-twisted and the line shapes do not have a completely absorptive shape. The phase-twisted shapes are explained by Figure 2, which shows that every peak has an unpaired subdiagram causing an imbalance between N- and P-type coherence; the imbalance disappears only when coherence between α and β has been destroyed. It is important to note that a partially dispersive peak shape in a 2D spectrum does not imply that the peak partially originates from a refractive index change; for example, dispersive line shapes are generated whenever a signal is truncated at the origin and may or may not be sensitive to refractive effects.[50]

The unpaired subdiagrams also cause the T-dependent variation in the peak shape, since all such subdiagrams evolve through $\alpha\beta$ or $\beta\alpha$ coherence during T. The signal modulation is caused by complex exponential factors, such as $\exp[-i\omega_{\beta\alpha}T]$ in eq 11, which decay exponentially with a rate of $\Gamma_{\beta\alpha}$ ($=4\gamma_{as}$). $\alpha\beta$ coherence causes an oscillating shape for peaks $DP_{\alpha\alpha0}$ and $DP_{\beta\beta0}$ which are elongated parallel and antiparallel to the diagonal at half and full periods, respectively;[51] in contrast, all four cross-peaks are elongated antiparallel to the diagonal at half period and parallel to the diagonal at full periods (a behavior noted previously for $CP_{\alpha\beta0}$ and $CP_{\beta\alpha0}$ in ref 51). Such oscillations in 2D peak shape have been experimentally observed in 2D electronic spectra.[35,36] The cause of these changes in shape is seen in its bare form for the "diagonal" excited state absorption peaks $DP_{\alpha\alpha2}$ and $DP_{\beta\beta2}$, which arise from a single subdiagram [$6d_4$ ($6d_3$) for $DP_{\alpha\alpha2}$ ($DP_{\beta\beta2}$)]. For $DP_{\alpha\alpha2}$ and $DP_{\beta\beta2}$, the complex-valued 2D peak shape is multiplied by $\exp[-i\Delta T]$ so that, at half period intervals, the real peak shape alternates between positive and negative phase-twisted absorption (both elongated antiparallel to the diagonal). At quarter and three-quarter periods, the imaginary peak shape transforms into the real peak shape and vice versa; the real 2D peak shapes are positive and negative phase-twisted dispersive lineshapes. The oscillating peak amplitude variation with T can also be seen by examining Figure 3 at high resolution (online); for the ESE/GSB diagonal peaks $DP_{\alpha\alpha0}$ and $DP_{\beta\beta0}$, the peak amplitude is maximum at full periods and minimum at half periods; all cross-peaks have maximum absolute amplitude at full periods and minimum at half periods; for the ESA diagonal peaks $DP_{\alpha\alpha2}$ and $DP_{\beta\beta2}$, as mentioned above, the real peak amplitude is alternatively positive and negative, modulated by the factor $\exp[-i\Delta T]$. The peak amplitude of the GSB/ESE diagonal peaks $DP_{\alpha\alpha0}$ and $DP_{\beta\beta0}$ is anticorrelated to the diagonal width.[51] For $T \gg 1/\Gamma_{\beta\alpha}$, the contribution from all the unpaired subdiagrams diminishes to zero and therefore the 2D peaks are no longer T dependent in amplitude and no longer phase twisted.

2. Ideal Spectrally Resolved Pump Probe Spectra. Figure 4 shows the undistorted spectrally resolved pump−probe spectrum corresponding to the 2D spectra of Figure 3. When integrated over the ω_τ dimension, the dispersive components in the real part of the 2D spectrum do not always cancel, despite the apparent overall N/P balance for integration over ω_τ in Figure 2. Absorptive line shapes are observed only at integer and "integer plus a half" periods of quantum beat oscillation. At half periods, ESA peaks diminish to near zero amplitude (the amplitude would be zero in the absence of damping) and the GSB/ESE peak intensities are minimized. Mathematically, the line shape is absorptive at half and full period because the real part of the full period 2D spectra is uncontaminated by the imaginary part of the full period 2D spectra. The physical origin is that phase evolution during T causes the refractive component of the nonlinear free induction decay to be in (or out) of phase with the probe and therefore change the probe spectrum at 1/4 and 3/4 period. At half period, the $DP_{\beta\beta2}$ and $CP_{\alpha\beta2}$ peaks sum to zero (and hence the negative peaks disappear in the SRPP spectrum) because oscillatory subdiagrams $6d_3$ from $DP_{\beta\beta2}$ and $5d_4$ from $CP_{\alpha\beta2}$ combine to cancel nonoscillatory subdiagrams $6d_1$ and $5d_1$ from $CP_{\alpha\beta2}$.

For each SRPP peak, both oscillatory subdiagrams have the same coherence during T ($\beta\alpha$ for peaks at $\omega_{2\alpha}$ and $\omega_{\beta0}$, $\alpha\beta$ for peaks at $\omega_{2\beta}$ and $\omega_{\alpha0}$). As a result, the SRPP peaks can have partially dispersive lineshapes. At quarter and three-quarter periods, all of the peaks show oscillations in the asymmetry about the center, which is hardly shifted. Although this is most obvious for the smaller negative ESA peaks in Figure 4, which have larger amplitude on the sides away from each other at a 1/4 period and larger amplitude toward each other at 3/4 period,

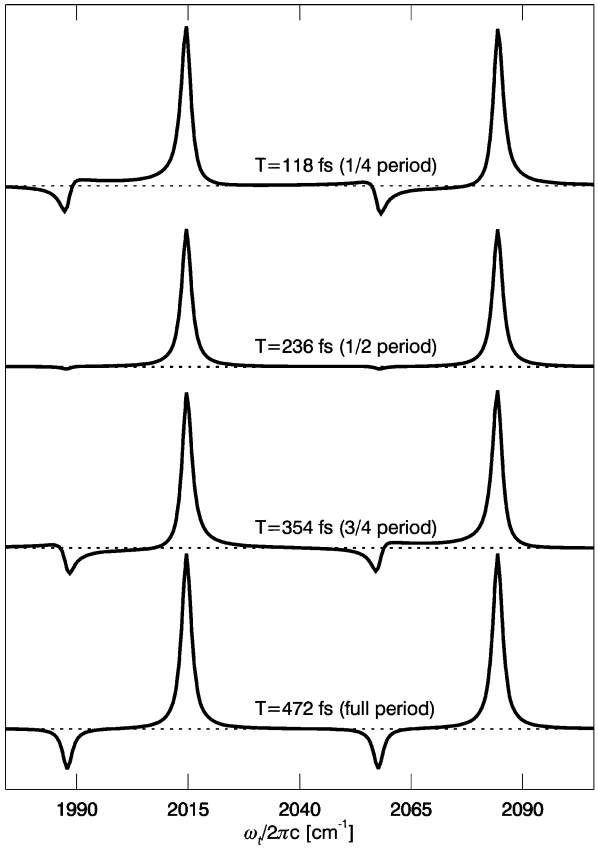

Figure 4. Ideal spectrally resolved pump−probe (SRPP) spectra shown at 118, 236, 354, 472 fs from the top to bottom. These times correspond to quarter periods of the quantum beat with period $2\pi/\Delta$. The SRPP spectra are obtained by integrating the 2D spectra in Figure 3 over the ω_τ dimension. There are small periodic oscillations in the amplitude of the largest peaks at $\omega_{\alpha 0}/2\pi c$ (2015 cm^{-1}) and $\omega_{\beta 0}/2\pi c$ (2084.8 cm^{-1}). The smaller excited state absorption peaks at $\omega_{2\beta}/2\pi c$ (1988.2 cm^{-1}) and $\omega_{2\alpha}/2\pi c$ (2058 cm^{-1}) are both 100% amplitude modulated (compare half and full periods) and periodically phase-twisted (the line shape is a mix of absorptive and dispersive lineshapes at 1/4 and 3/4 period).

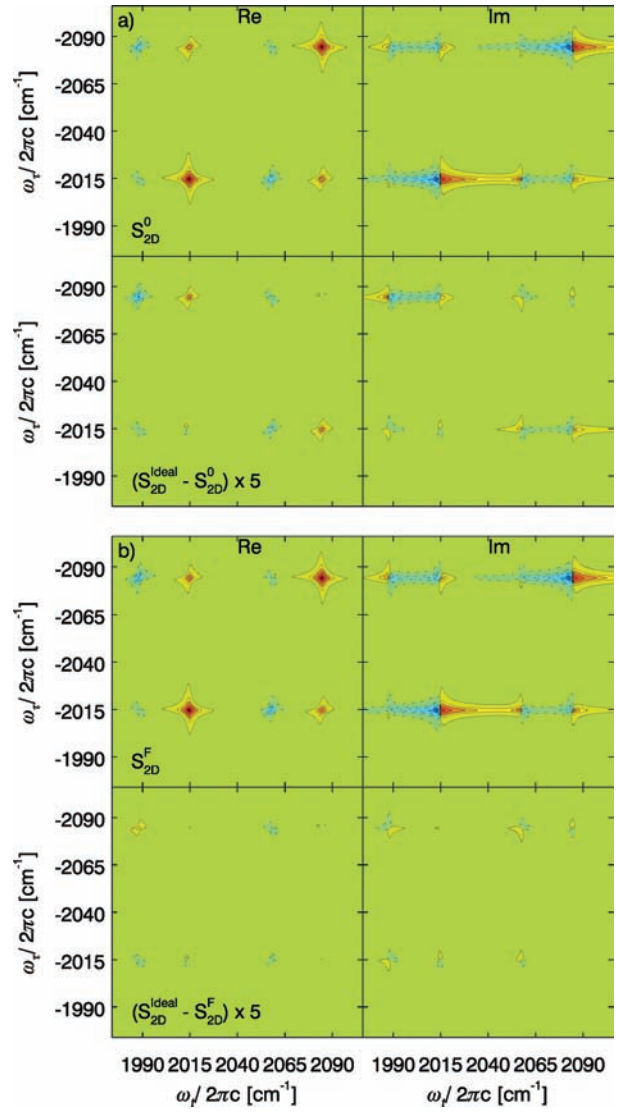

Figure 5. Directional filtering distortions. (a) Effect of directional filter for an infinitely thin sample. The maximum error is 0.051 and the rms error is 0.0017 times the height of the strongest peak in the same scale. (b) Spectra corrected for directional filtering distortion ($\hat{S}^F_{2D}$), using eq 8. Maximum error = 0.011, rms error = 0.00062. For both (a) and (b), the calculated real (left column) and imaginary (right column) part of the distorted ($\hat{S}$2D, top panels) and the difference spectra ($\hat{S}^{Ideal}_{2D} - \hat{S}^{2D}$, bottom panels) are shown. The four-level system and 3DFT calculation parameters are the same as those in Figure 3, but the beam geometry is characterized by the beam waist, $w_0 = 150$ μm and the external crossing angle $2\theta = 2\phi = 10°$. The relaxation time is $T = 472$ fs. Contour levels are −90, −80, −70, −60, −50, −40, −30, −20, −10, −7, −4, −1, 1, 4, 7, 10, 20, 40, 60, 80, 90% with dotted contour indicating negative amplitude. The difference spectra are multiplied by 5 so that the third positive contour (10%) represents a 2% reduction in amplitude through directional filtering.

the low amplitude wings of the larger positive GSB/ESE peaks show the same trend. The lines are symmetrical at half and full periods. This asymmetry oscillation is clearly linked to asymmetries in the 2D peak shapes at 1/4 and 3/4 period in Figure 3. Although similar amplitude oscillations have been reported previously in spectrally resolved pump−probe experiments,[15,52] the partially dispersive line shapes at some time delays may be below the experimental noise level. To our knowledge, this prediction of phase-twisted line shapes in spectrally resolved pump−probe transients awaits experimental confirmation.

3. Directional Filter Distortion. The physical origin of the directional filter is made clear in ref 23. Briefly, the variation in wave vector between different frequency components of a beam traveling in a single direction causes different components of the signal to have varying overlap with the detection beam. Figure 5 illustrates the distortion by directional filtering (a: $\hat{S}^0_{2D}$) and the result of the transformation in eq 8 (b: $\hat{S}^F_{2D}$) for an infinitely thin sample at $T = 472$ fs (full period). For $\hat{S}^0_{2D}$ and $\hat{S}^F_{2D}$, the real and imaginary part (top panels) and the difference spectra to S^{Ideal}_{2D} (bottom panels) are shown. The difference spectra are multiplied by 5. For all peaks, the intensity is reduced by directional filtering in $\hat{S}^0_{2D}$. There is minimal reduction for $DP_{\alpha\alpha 0}$ and $DP_{\beta\beta 0}$ (<1%). The smaller peaks, $DP_{\alpha\alpha 2}$ and $DP_{\beta\beta 2}$, see ∼17% and 18% reduction in their amplitudes, respectively. $CP_{\beta\alpha 0}$ and $CP_{\alpha\beta 0}$ see a similar reduction in their amplitudes of ∼14%. On the other hand, $CP_{\beta\alpha 2}$ and $CP_{\alpha\beta 2}$, which have intrinsically the same peak shape and amplitude, see different amounts of reduction by directional filtering: $CP_{\beta\alpha 2}$ is reduced by ∼23% and $CP_{\alpha\beta 2}$ reduced by ∼8%. This occurs because the distances from the diagonal are quite different.

Yetzbacher et al.[23] showed that for a two-level system, the dimensionless parameter $[(\Delta\omega)w_0 \sin(\beta)/c]^2$ gives a useful estimate of the extent of the directional filtering distortion for a peak shape, where $\Delta\omega$ is the peak width. This dimensionless parameter does not give a good estimate of the filtering for widely separated peaks in a multilevel system using the peak separation as $\Delta\omega$; individual peaks experience varying levels of distortion. The most accurate way to account for the

directional filter distortion, $\Phi^{(3)}$, proceeds subdiagram by subdiagram. Because the directional filtering is nearly constant over the range of the line width ($\sim$2 cm^{-1}), attenuation by filtering is almost uniform over the width of each peak; each subdiagram's contribution to the 2D spectrum may therefore be multiplied by a $\Phi^{(3)}$ calculated "on resonance" for that subdiagram using $\omega_a - \omega_b$ and $\omega_a - \omega_c$ in eq 6. For example, for subdiagram $6d_3$, $\omega_a - \omega_b = \Delta$ and $\omega_a - \omega_c = d$; $\Phi^{(3)}$ is estimated to cause $\sim$17.2% reduction in the intensity of $DP_{\beta\alpha 2}$, which matches the reduction of $\sim$16.7% in the 3DFT simulation within convergence error. The orientational factor weighted averages of $\Phi^{(3)}$ for the remaining peaks agree with the 3DFT simulation within 1%. (The above approach can be used, along with the appropriate directional filter for SRPP given below eq 6, to estimate the directional filter distortions of the SRPP transients; all quantum beats are reduced in amplitude.[23])

A complete characterization of $\Phi^{(3)}$ on individual peaks is only possible if all coherence pathways are known, making the diagram by diagram approach dependent on models. Experimentally such knowledge may not always be available, rendering such an approach less applicable. The transformation in eq 8 uses ω_τ in place of ω_a and ω_b, and ω_t in place of ω_c in eq 6; this becomes exact in the limit of large T when no $\alpha\beta$ coherence remains. When the transformation of eq 8 is applied to the whole 2D spectrum to undo the directional filter distortion, the fractional errors are reduced to a $\sim$1% distortion of $CP_{\beta\alpha 0}$ and $CP_{\alpha\beta 0}$, $\sim$5% of $CP_{\beta\alpha 2}$, and $\sim$3% of $CP_{\alpha\beta 2}$. In $DP_{\alpha\alpha 2}$ ($DP_{\beta\beta 2}$) the transformation reduces the fractional error from 18% to 16% (16% to 14%). The absolute maximum error over the plotted region is reduced from 0.051 to 0.011, and rms error is reduced from 0.0017 to 0.00062 (relative to the strongest real peak). At $T = 472$ fs, the discrepancy between the transformed ($\hat{S}^{F}_{2D}$) and ideal ($\hat{S}^{Ideal}_{2D}$) spectra is therefore due to coherence. At $T = 4720$ fs ($\sim 2 \times$ dephasing time), the transformation reduces the fractional error to less than 1% for all peaks. At this large value of T, the absolute maximum error is reduced from 0.046 to 0.0013 and rms error from 0.0014 to 8.6×10^{-5}. These errors are well within those expected from convergence and the finite value of $\Gamma_{\alpha\beta}T$.

4. Resonant Absorption and Dispersion Distortion. The complex refractive index of the sample quantifies how it absorbs and disperses excitation pulses and the signal, causing distortions from the ideal response. Figure 6 illustrates the absorptive/dispersive distortion at $T = 472$ fs with a collinear beam geometry. The real part of the distorted spectrum ($\hat{S}^{0}_{2D}$, top panel) at $\alpha_{max}L = 0.5$ ($OD_{max} \sim 0.43$), the transformed spectrum ($\hat{S}^{++}_{2D}$, middle panel) and the difference ($\hat{S}^{Ideal}_{2D} - \hat{S}^{++}_{2D}$, bottom panel) are shown. The difference spectra are multiplied by 5. The amplitudes of $DP_{\alpha\alpha 2}$, $DP_{\beta\beta 2}$, $CP_{\beta\alpha 2}$, and $CP_{\alpha\beta 2}$ increase by $\sim$84% relative to $DP_{\alpha\alpha 0}$ ($DP_{\beta\beta 0}$) upon distortion. $DP_{\alpha\alpha 0}$, $DP_{\beta\beta 0}$, $CP_{\beta\alpha 0}$, and $CP_{\alpha\beta 0}$ experience the same level of attenuation; relative to each other, these peak heights stay the same in the distorted spectrum (the ratio of $CP_{\beta\alpha 0}$ to $DP_{\beta\beta 0}$ is $\sim$1:5). The absorptive/dispersive distortion leads to peak broadening. In $DP_{\alpha\alpha 0}$ and $DP_{\beta\beta 0}$, there is $\sim$13% more broadening in the ω_t dimension than in the ω_τ dimension (at the 4% contour). $CP_{\beta\alpha 0}$ and $CP_{\alpha\beta 0}$ broaden approximately equally in both dimensions (at the 4% contour) and so maintain similar aspect ratios upon distortion. In $CP_{\beta\alpha 2}$, $CP_{\alpha\beta 2}$, $DP_{\alpha\alpha 2}$, and $DP_{\beta\beta 2}$, the broadening results in elongation along the ω_τ dimension. When the distorted and undistorted peaks are normalized to their own maximum amplitudes, the aspect ratio (ω_τ dimension:ω_t dimension) increases $\sim$30% for $CP_{\beta\alpha 2}$ and $CP_{\alpha\beta 2}$ and $\sim$26% for $DP_{\alpha\alpha 2}$ and $DP_{\beta\beta 2}$ upon distortion.

Absorptive attenuation is greatest at the peak center and smaller at the wings, so the peaks are broadened. Similarly, nonlinear transitions overlapping the linear absorption spectrum (with peaks at $\omega_{\alpha 0}$ and $\omega_{\beta 0}$) see attenuation whereas those without overlap are unattenuated. The GSB and ESE pathway signals ($DP_{\alpha\alpha 0}$, $DP_{\beta\beta 0}$, $CP_{\beta\alpha 0}$, and $CP_{\alpha\beta 0}$), therefore, see attenuation at both excitation (ω_τ) and detection (ω_t) frequencies. The ESA pathway signals ($DP_{\alpha\alpha 2}$, $DP_{\beta\beta 2}$, $CP_{\beta\alpha 2}$, and $CP_{\alpha\beta 2}$), on the other hand, only see attenuation at the excitation frequencies and not at the detection frequencies. Consequently, the GSB and ESE peaks are broadened in both dimensions and thus retain similar aspect ratios whereas the ESA peaks are broadened only in the ω_τ dimension resulting in the vertically elongated peak shape.

The transformation to $\hat{S}^{++}_{2D}$ reduces the absolute maximum error from 0.31 to 0.076 and rms error from 0.023 to 0.0033. After the transformation to $\hat{S}^{++}_{2D}$ there is a residual broadening in $DP_{\alpha\alpha 0}$, $DP_{\beta\beta 0}$, $CP_{\beta\alpha 0}$, and $CP_{\alpha\beta 0}$ with fractional amplitude errors of $\sim$7% for DP and $\sim$12% for CP. There is a large decrease in fractional error for the amplitudes of $DP_{\alpha\alpha 2}$, $DP_{\beta\beta 2}$, $CP_{\beta\alpha 2}$, and $CP_{\alpha\beta 2}$ from $\sim$84% to $\sim$14%. At $T = 4720$ fs, the absolute maximum error further decreases to 0.023 and rms error to 0.00067; in all peaks, the relative errors are <3%. In the limit that all the coherence is destroyed, the error in $\hat{S}^{++}_{2D}$ becomes zero. The difference between $\hat{S}^{Ideal}_{2D}$ and $\hat{S}^{++}_{2D}$ in the bottom panel of Figure 6 shows two important trends: first, except for the diagonal peaks used to normalize the two spectra, the absolute magnitude of every peak is overestimated by $\hat{S}^{++}_{2D}$; second, every peak is distorted in such a way as to reduce its phase twist (the phase twist of the difference is opposite the phase twist of the peak).

5. Combined Distortion. The 2D spectrum was simulated with a 3DFT algorithm for $\alpha_{max}L = 0.25$ ($OD_{max} \sim 0.22$), external crossing angles of $2\theta = 2\phi = 10°$, and a beam waist of $w_0 = 150$ μm. These are approximately the conditions realized in the experiments by Khalil et al.[12,15] The top panels of Figure 7 show the real part of the 2D spectra at $T = 4720$ fs (a,$\hat{S}^{0}_{2D}$), the result of transformation to correct for absorptive/dispersive distortion (b,$\hat{S}^{++}_{2D}$), and the result of transformation to correct for directional filtering applied to $\hat{S}^{++}_{2D}$ (c,$\hat{S}^{F++}_{2D}$). The bottom panels show differences from the ideal 2D spectrum, multiplied by 5.

In $\hat{S}^{0}_{2D}$, the absorptive/dispersive distortion dominates for $DP_{\alpha\alpha 0}$ and $DP_{\beta\beta 0}$ (directional filtering is negligible for these peaks); the peak amplitudes decrease and the width increases in both dimensions. The rest of the peaks are significantly distorted by both absorption/dispersion and directional filtering. The absorptive/dispersive distortion reduces $CP_{\beta\alpha 0}$ and $CP_{\alpha\beta 0}$ amplitudes to the same extent as $DP_{\alpha\alpha 0}$ and $DP_{\beta\beta 0}$. However, $CP_{\beta\alpha 0}$ and $CP_{\alpha\beta 0}$ are further suppressed by directional filtering, so that when the spectrum is normalized to $DP_{\alpha\alpha 0}$, the distorted peaks have smaller amplitudes compared to $\hat{S}^{Ideal}_{2D}$; at the peak center, $Re(\hat{S}^{Ideal}_{2D} - \hat{S}^{0}_{2D})$ has a small positive value, rather than zero as for the absorptive/dispersive distortion only. For the ESA peaks ($DP_{\alpha\alpha 2}$, $DP_{\beta\beta 2}$, $CP_{\beta\alpha 2}$, and $CP_{\alpha\beta 2}$), the absorptive/dispersive distortion leads to an elongation of the peak shape in the ω_τ dimension and increase in the relative peak amplitudes compared to the GSB/ESE peaks ($DP_{\alpha\alpha 0}$, $DP_{\beta\beta 0}$, $CP_{\beta\alpha 0}$, and $CP_{\alpha\beta 0}$). This gain in the relative amplitudes due to the absorptive/dispersive distortion is partially canceled by a decrease in the relative amplitudes due to the directional filtering; the combined distortions result in reduced overall distortion compared to the absorption/dispersion only spectra (see parts a and b of Figure 6).

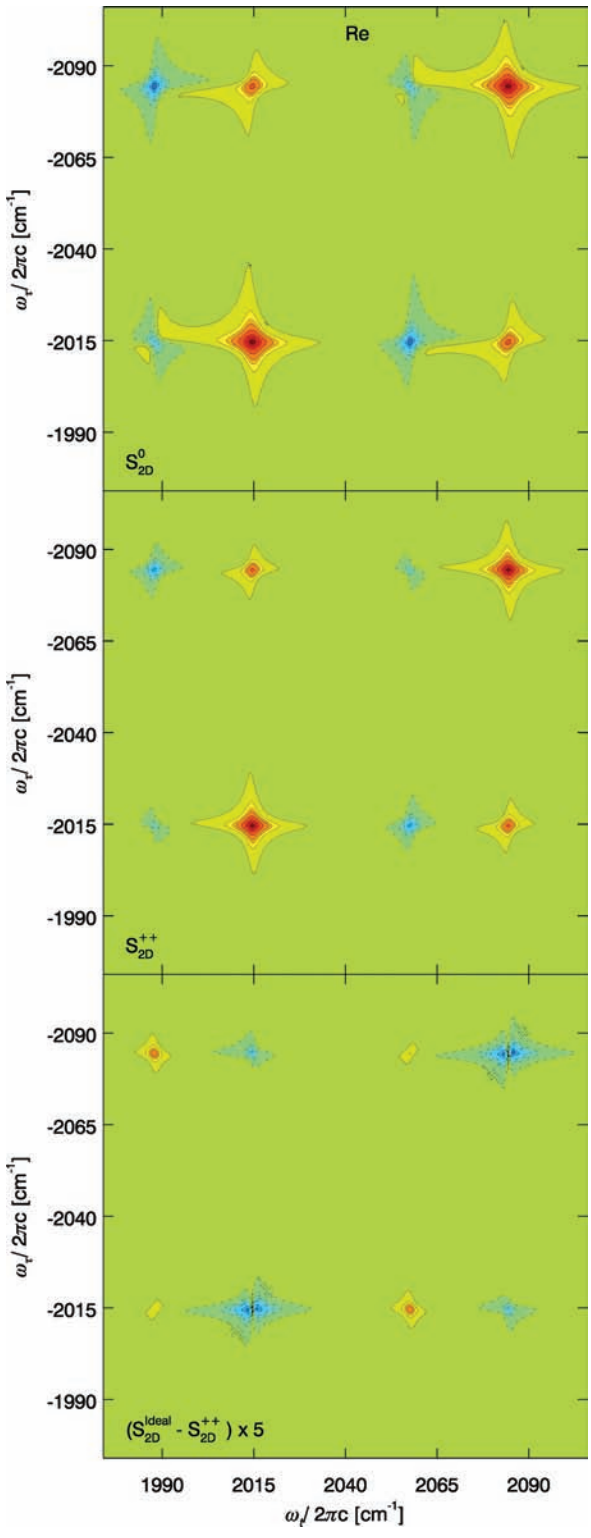

Figure 6. Resonant absorption and dispersion distortions. The calculated real part of the distorted ($\hat{S}^0_{2D}$, top panel), transformed ($\hat{S}^{++}_{2D}$, middle panel), and the difference spectra ($\hat{S}^{Ideal}_{2D} - \hat{S}^{++}_{2D}$, bottom panel) with a collinear beam geometry at $\alpha_{max}L = 0.5$ ($OD_{max} \sim 0.43$) are shown at mixing time $T = 472$ fs. Maximum and rms error in the distorted spectrum are 0.31 and 0.023. The maximum and rms error in the transformed spectrum are 0.076 and 0.0033. The four-level system and 3DFT calculation parameters are the same as in Figure 3. Contour levels are −90, −80, −70, −60, −50, −40, −30, −20, −10, −7, −4, −1, 1, 4, 7, 10, 20, 40, 60, 80, 90% with dotted contours indicating negative amplitude. The difference spectra are multiplied by 5 so that the third positive contour (10%) represents a 2% reduction through absorption/dispersion.

Parts a−c of Figure 7 show that at large T, when all coherence is destroyed, successive transformations to correct for absorptive/dispersive distortions and then for directional filtering are able to recover a spectrum that deviates from $\hat{S}^{Ideal}_{2D}$ by <2% in absolute maximum error (within convergence error). In Table 2, absolute maximum errors, rms errors, and fractional errors on each peak for $\hat{S}^0_{2D}$, $\hat{S}^{++}_{2D}$, and $\hat{S}^{F++}_{2D}$ are tabulated for $T = 118$, 236, 472, and 4720 fs. The worst error in $\hat{S}^{F++}_{2D}$ is 6% of the largest peak, but 26% of the ideal peak height for $DP_{\alpha\alpha 2}$ at $T = 118$ fs. This error is less than that in $\hat{S}^0_{2D}$ and equal to that for $\hat{S}^{++}_{2D}$. There is one peak where $\hat{S}^{F++}_{2D}$ produces a larger error than $\hat{S}^{++}_{2D}$—for $CP_{\alpha\beta 2}$ the error increases by up to 5%. At early times, $\hat{S}^{F++}_{2D}$ and $\hat{S}^{++}_{2D}$ are comparable in maximum and rms error but $\hat{S}^{F++}_{2D}$ has smaller errors for most peaks. Of $\hat{S}^0_{2D}$, $\hat{S}^{++}_{2D}$ and $\hat{S}^{F++}_{2D}$, $\hat{S}^{F++}_{2D}$ seems overall to be closest to the ideal 2D spectrum at early times. $\hat{S}^{F++}_{2D}$ is superior in all respects at later times.

V. Discussion

In the ideal spectra, the red shift from cross anharmonicity (or a biexciton shift) separates the ESA peaks from the GSB and ESE peaks. As a result, a scanning procedure to balance N-type ("echo") and P-type ("anti-echo") coherence pathways, commonly used in NMR, does not necessarily lead to a balancing of N- and P-type coherence in optical 2D spectra; every peak is inherently imbalanced and thus phase-twisted as long as the $\alpha\beta$ level coherence survives.[12] The extent of the phase-twist depends on the orientational average (and thus on the polarization of the excitation pulses). For $T < (1/\Gamma_{\alpha\beta})$, the phase twist is severe. The same coherence pathways that cause the phase twist quantum beats are also the origin of amplitude quantum beats with T in the 2D spectra; as illustrated by eq 11, for subdiagram $6d_3$ the complex time evolution interconverts real and imaginary 2D peak shapes until $\alpha\beta$ coherence dephasing is complete. Similar periodic oscillations of the ratio of the diagonal to antidiagonal widths that are anticorrelated with oscillation of the peak amplitude have been observed in 2D electronic spectra[35,36] and simulated with models that incorporate dynamical inhomogeneous broadening.[51] The calculations presented here show that this effect is present even for pure homogeneous broadening. This is especially so in ESA peaks since the pathways that cause the phase twist either accounts for the peak entirely ($DP_{\alpha\alpha 2}$ and $DP_{\beta\beta 2}$) or contributes 1/3 of the amplitude ($CP_{\alpha\beta 2}$ and $CP_{\beta\alpha 2}$). Despite N/P balance, the associated SRPP spectra have excited-state absorptions that are modulated in both amplitude and absorptive/dispersive line shape character.

The periodic changes in peak shape caused by the phase-twist quantum beats associated with resolved 2D cross-peaks can be experimentally distinguished from those caused by unresolved vibrational wavepacket motion within a 2D peak shape. Vibrational wavepacket motion broadens diagonal 2D peak shapes along the diagonal at multiples of the vibrational period and broadens them along the antidiagonal halfway through each vibrational period,[34] an effect recently seen by Ogilvie and co-workers.[53] In contrast, phase-twist quantum beats cause diagonal 2D peaks to broaden along the diagonal at halfway through each quantum beat period and along the antidiagonal at each complete period. More complicated electronic 2D peak shape oscillations[54] might involve both effects.

Khalil et al.[15] noted that the phase-twist of peak $DP_{\beta\beta 2}$ (peak 5 in ref 15) is sensitive to coherence transfer. $\alpha\beta \leftrightarrow \beta\alpha$ coherence transfer would ultimately replace $\exp[-i\omega_{\beta\alpha}T]$ in eq 11 with $\cos(\omega_{\beta\alpha}T)$, so that the periodic absorptive/dispersive peak shape oscillation for $DP_{\beta\beta 2}$ and $DP_{\alpha\alpha 2}$ without coherence

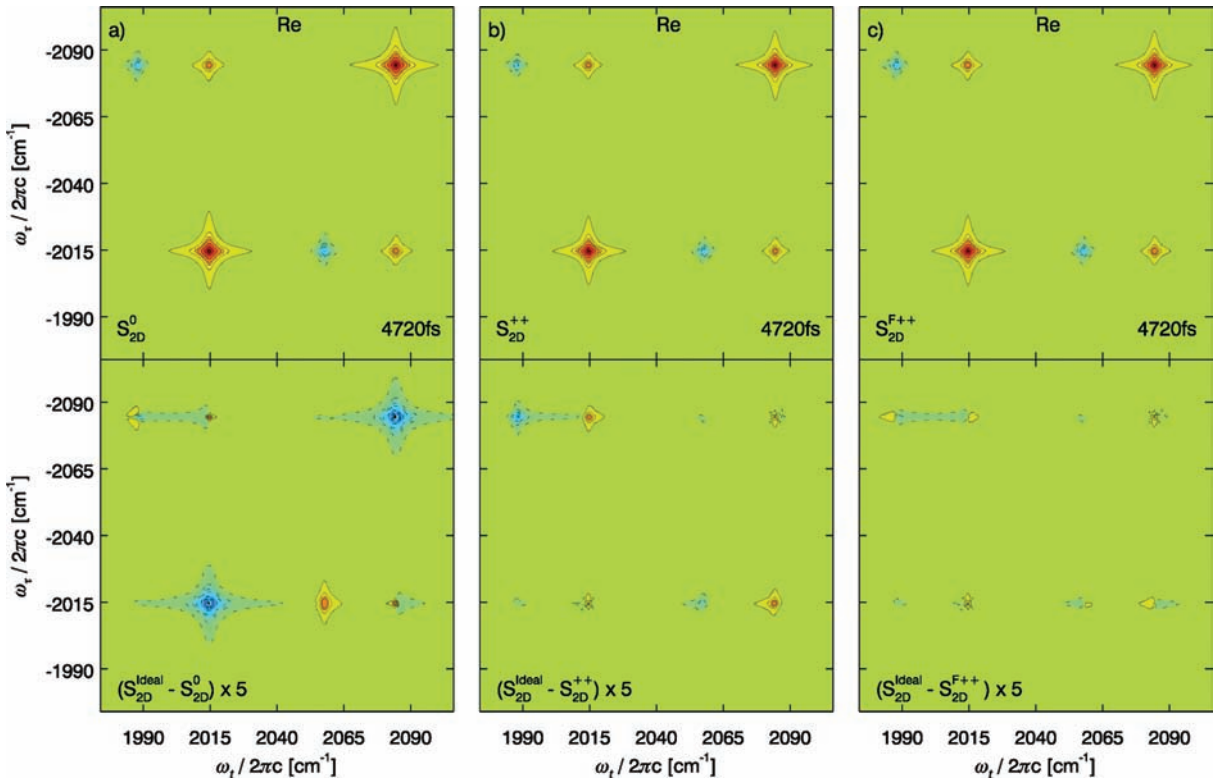

Figure 7. Simulated 2D spectrum with absorptive/dispersive propagation distortions and directional filtering. (a) The real part of $\hat{S}^0_{2D}$, (top) and difference ($\hat{S}^{Ideal}_{2D} - \hat{S}^0_{2D}$), (bottom). (b) The real part of the transformed spectrum to correct for absorption/dispersion distortion ($\hat{S}^{++}_{2D}$, top) and difference spectrum ($\hat{S}^{Ideal}_{2D} - \hat{S}^{++}_{2D}$), (bottom). (c) The real part of transformed spectrum to correct for both the absorption/dispersion and directional filter distortions $\hat{S}^{F++}_{2D}$, (top) and the difference spectrum ($\hat{S}^{Ideal}_{2D} - \hat{S}^{F++}_{2D}$), (bottom). The absolute maximum error is reduced from 0.11 ($\hat{S}^0_{2D}$) to 0.048 ($\hat{S}^{++}_{2D}$) to 0.016 ($\hat{S}^{F++}_{2D}$) and rms error from 0.0071 ($\hat{S}^0_{2D}$) to 0.0016 ($\hat{S}^{++}_{2D}$) to 0.00069 ($\hat{S}^{F++}_{2D}$). The four-level system and 3DFT calculation parameters are the same as those in Figure 3, but the beam geometry is characterized by beam waist, w_0= 150 μm and the external crossing angle $2\theta = 2\phi = 10°$. Optical density is $\alpha_{max}L = 0.25$ ($OD_{max} \sim 0.22$). The relaxation time is $T = 4270$ fs. Contour levels are −90, −80, −70, −60, −50, −40, −30, −20, −10, −7, −4, −1, 1, 4, 7, 10, 20, 40, 60, 80, 90% with dotted contours indicating negative amplitude. The difference spectra are multiplied by 5 so that the third positive contour (10%) represents a 2% reduction through combined distortion.

TABLE 2: Max and rms Errors within the Plotted Range and Errors on Individual Peaks for Combined Distortion Spectrum ($\hat{S}^0_{2D}$), Transformed Spectrum to Correct for Absorption/Dispersion Distortion ($\hat{S}^{++}_{2D}$), and Transformed Spectrum to Correct for Both the Absorption/Dispersion and Directional Filter Distortion ($\hat{S}^{F++}_{2D}$) at T = 118, 236, 472, and 4720 fs[a]

	1/4 period (118 fs)			1/2 period (236 fs)			full period (472 fs)			4720 fs		
	S^0_{2D}	S^{++}_{2D}	S^{F++}_{2D}	S^0_{2D}	S^{++}_{2D}	S^{F++}_{2D}	S^0_{2D}	S^{++}_{2D}	S^{F++}_{2D}	S^0_{2D}	S^{++}_{2D}	S^{F++}_{2D}
max error	0.16	0.060	0.060	0.15	0.056	0.056	0.14	0.045	0.045	0.11	0.048	0.016
rms error	0.0099	0.0028	0.0028	0.0096	0.0026	0.0025	0.0092	0.0023	0.0022	0.0071	0.0016	7×10^{-4}
$CP_{\beta\alpha 2}$	0.12	0.23	−0.14	0.14	0.30	0.11	−0.091	0.18	−0.14	0.10	0.28	0.057
$CP_{\beta\alpha 0}$	0.11	0.12	0.087	0.091	0.091	0.11	0.091	0.096	0.089	0.15	0.15	0.040
$DP_{\beta\beta 2}$	0.25	0.20	0.18	0.19	−0.077	0.061	−0.12	0.14	0.12	0.36	0.29	0.29*
$DP_{\beta\beta 0}$	0.13	0.059	0.059	0.12	0.055	0.055	0.11	0.044	0.044	0.074	0.012	0.012
$DP_{\alpha\alpha 2}$	0.31	0.26	0.26	0.21	0.091	0.078	−0.17	0.15	0.13	0.54	0.43	0.43*
$DP_{\alpha\alpha 0}$	0.13	0.057	0.057	0.13	0.054	0.054	0.12	0.041	0.042	0.077	0.012	0.012
$CP_{\alpha\beta 2}$	−0.32	−0.061	−0.11	−0.41	−0.12	−0.17	−0.26	0.031	−0.051	−0.19	0.077	0.033
$CP_{\alpha\beta 0}$	0.12	0.13	0.077	0.091	0.092	0.093	0.099	0.10	0.080	0.16	0.16	0.038

[a] Errors on each individual peak are calculated as fractional differences in amplitude when compared to the undistorted amplitude for that peak. Negative signs indicate that the amplitude increases upon distortion. The two errors marked with an asterisk occur for peaks with amplitudes below 1% (smaller than the convergence error of 2%)—too weak to be visible in Figure 7.

transfer would become a periodic pure amplitude modulation of the peak shape. As signatures of rapid coherence transfer have been observed in some 2D-IR experiments in solution[15,55] and in time-resolved electronic spectroscopy,[56] oscillating peak shapes in 2D and oscillating asymmetry in SRPP (or their absence) are likely to provide useful information on coherence transfer phenomena. It is quite interesting that ESA peaks in SRPP can reveal coherence transfer rates through the decay of periodic oscillations in asymmetry.

In their calculations of absolute value 2D photon echo spectra from multilevel systems, Keusters and Warren[24,25] found that the absorptive/dispersive distortions significantly reduce the amplitudes of peaks generated by the GSB and ESE coherence pathways. The results here are similar; the reduction in amplitude is higher for larger absorption and so the distortion broadens the peak widths. The ESA peaks experience attenuation only at excitation frequencies and not at detection frequencies, so the broadening only occurs along the ω_τ axis at constant ω_t, resulting in an elongation in the ω_τ dimension. As noted by Keuster and Warren[24,25] and Yetzbacher et al.,[23] such distortions depend on the details of the relaxation model. The phase-resolved 2D spectra calculated here reveal that resonant absorption and dispersion also reduces the phase twist of

all the peaks in the 2D spectrum. This can be quantitatively explained by a scrambling of the *a*, *b* pulse ordering allowed by the linear free induction decay that trails after each pulse.[21] This observation that absorptive/dispersive propagation distortion reduce the phase twist of 2D peak is important because loss of phase twist is a signature of coherence transfer.[15] This reduction of phase twist is not corrected by transformation to $\hat{S}_{2D}^{++}$. In addition, the two GSB/ESE diagonal peaks ($DP_{\alpha\alpha0}$ and $DP_{\beta\beta0}$) in $\hat{S}_{2D}^{++}$ exhibit a residual distortion that strongly resembles the square of the dispersive 2D peak shape. Nevertheless, $\hat{S}_{2D}^{++}$ reduces the disagreement between ideal and experimentally distorted 2D spectra and is recommended to correct for absorptive/dispersive propagation distortion of experimental 2D spectra.

The directional filter affects the cross peaks and ESA peaks significantly, but not the main diagonal peaks ($DP_{\alpha\alpha0}$ and $DP_{\beta\beta0}$). This differential effect may be understood by considering the effect on individual coherence pathways that contribute to peaks; from eq 6 its effect is to attenuate the amplitudes of diagrams based on $\omega_a - \omega_b$ and $\omega_a - \omega_c$. The directional filtering effect causes the amplitudes of $CP_{\alpha\beta2}$ and $CP_{\beta\alpha2}$ (which are equal in ideal 2D spectra and in 2D spectra with absorptive/dispersive pulse propagation distortions) to differ. These effects are quantified, under conditions which simulate the experiment of refs 11, 12, and 15 in Table 2. The peak height changes for $\hat{S}_{2D}^{0}$ at a full quantum beat period show that, relative to the diagonal peaks, $CP_{\alpha\beta2}$ grows by 26% while $CP_{\beta\alpha2}$ grows by 9%. Therefore $CP_{\alpha\beta2}$ should be about 15% stronger than $CP_{\beta\alpha2}$ at a full period. This unequal net growth of the two cross-peaks relative to the diagonal peaks arises because absorption equally enhances both cross-peaks relative to the diagonal peaks, but directional filtering suppresses $CP_{\beta\alpha2}$ more strongly than $CP_{\alpha\beta2}$. At a quarter period, the amplitude of $CP_{\alpha\beta2}$ is 50% larger than $CP_{\beta\alpha2}$; $CP_{\alpha\beta2}$ is consistently larger than $CP_{\beta\alpha2}$. The above calculations predict that directional filtering distortions should be detectable in the experimental data of ref 15.

The experimental real 2D correlation spectrum in Figure 7 of ref 15 shows three contours for $CP_{\alpha\beta2}$ (peak 4′ of refs 11 and 15) and two for $CP_{\beta\alpha2}$ (peak 4 of refs 11 and 15). Although the relative cross-peak amplitudes might be affected by coherence and population transfer, differences in the forward and backward rates were constrained by detailed balance so that the simulations in Figure 7 of ref 15 yielded four contours (at 3.3% spacing) for both cross-peaks 4 and 4′. In contrast, Figure 2 of ref 15 shows experimental absolute value rephasing 2D spectra in which $CP_{\alpha\beta2}$ consistently has one more contour (spaced at 5% of the maximum of $DP_{\alpha\alpha0}$) than $CP_{\beta\alpha2}$. The above observations suggest that directional filtering accounts for the unequal amplitudes of these two cross-peaks. For more direct comparison to the rightmost experimental 2D spectrum in Figure 2 of ref 15, Figure 8 shows slices through the calculated absolute value "rephasing" 2D spectrum [the absolute value of the complex-valued 2D spectrum from a scan covering only positive τ after coherence relaxation ($T = 4270$ fs)]. The slices at $\omega_\tau/2\pi c = -2014.6$ and -2084.4 cm^{-1} show that $CP_{\alpha\beta2}$ should be one 5% contour above $CP_{\beta\alpha2}$ because of directional filtering. Although directional filtering might be modified by the coherence and population transfer processes neglected in calculating Figure 8, this result agrees with the experiment.

When the absorption/dispersion and directional filtering distortions are simultaneously present, they partially cancel each other out for ESA peaks. The errors in $\hat{S}_{2D}^{++}$ and $\hat{S}_{2D}^{F++}$ are almost comparable at small T when there is coherence; for seven out of eight peaks, $\hat{S}_{2D}^{F++}$ at 1/4 period performs as well as or better than $\hat{S}_{2D}^{++}$; for three out of those seven peaks, $\hat{S}_{2D}^{F++}$ does better

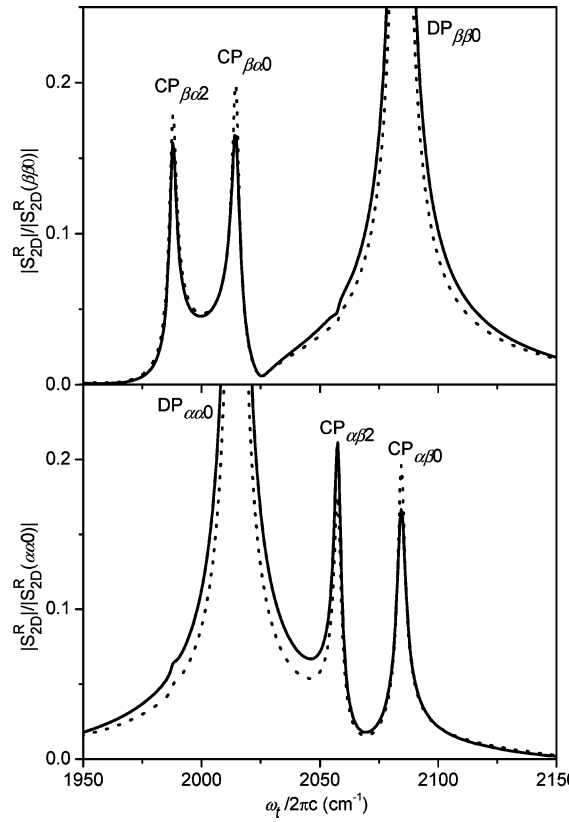

Figure 8. Slices through the ideal (dashed) and distorted (solid) absolute value "rephasing" 2D spectrum at relaxation time $T = 4270$ fs for $\omega_\tau = -2084.4$ cm^{-1} (top) and $\omega_\tau = -2014.6$ cm^{-1} (bottom) as a function of ω_t. The four-level system, 3DFT calculation, and experimental parameters are the same as in Figure 7. For the "rephasing" 2D spectrum, $\hat{S}_{2D}^{R}$, only the positive τ (N-type, "echo" subdiagrams on the right side of each column in Figure 2) 2D signal is included in calculating complex-valued 2D spectra using the recipe for $\hat{S}_{2D}^{0}$. The vertical axis for each slice is normalized to the diagonal peak on that slice (both diagonal peaks have the same amplitude). These two slices show the differential suppression of $CP_{\beta\alpha2}$ and enhancement of $CP_{\alpha\beta2}$ (relative to the diagonal peaks) through the combined action of absorption/dispersion and directional filtering.

than $\hat{S}_{2D}^{++}$. Similar conclusions hold at waiting times of 1/2 and full period. Finally, $\hat{S}_{2D}^{F++}$ is superior to $\hat{S}_{2D}^{++}$ when all coherence has decayed at large waiting times T. The caveat to recommending $\hat{S}_{2D}^{F++}$ as the preferred representation of experimental 2D spectra is that unlike the transformation from $\hat{S}_{2D}^{0}$ to $\hat{S}_{2D}^{++}$, which relies mainly on the complex refractive index $\hat{n}(\omega)$, correction of $\hat{S}_{2D}^{++}$ to $\hat{S}_{2D}^{F++}$ relies on the knowledge of not only the beam waist as a function of frequency but also assumptions about the full spatial intensity profile and the frequency-dependent spatial phase in the excitation fields, $E(r,\omega)$. These quantities are usually approximately known for near transform-limited pulses with pulse durations of many optical cycles.

We conclude the discussion by pointing out that some distortions of the 2D spectra will suggest relatively harmless counterbalanced misinformation about the model while others can conspire to mislead. Although $\Phi^{(3)}$ is not directly affected by beam polarization, directional filtering can distort the polarization dependence of a 2D peak through differential suppression of different subdiagrams that have distinct polarization-dependent orientational averages. For example, the ZZYY/ZZZZ amplitude ratios for $CP_{\alpha\beta2}$ and $CP_{\beta\alpha2}$ are identical in the ideal "rephasing" 2D spectrum of the model, but directional filtering distorts them in opposite directions while those of $CP_{\alpha\beta0}$ and $CP_{\beta\alpha0}$ are unchanged. With the correct model, the angles between transition dipoles determined using all four

cross-peaks might be fairly accurate even without consideration of directional filtering. In contrast, the peak $CP_{\beta\alpha 2}$ is more sensitive to $|\vec{\mu}_{2\beta}|$ while $CP_{\alpha\beta 2}$ is more sensitive to $|\vec{\mu}_{2\alpha}|$, so that least-squares fitting could alter the ratio $|\vec{\mu}_{2\beta}|/|\vec{\mu}_{2\alpha}|$ to fit a directional filtering distortion. Similarly, the ratios $|\vec{\mu}_{2\beta}|/|\vec{\mu}_{\beta 0}|$ and $|\vec{\mu}_{2\alpha}|/|\vec{\mu}_{\alpha 0}|$ are all enhanced by absorption, so these parameters could be quantitatively distorted in a least-squares fit. Although the redundancy in 2D spectra can sometimes minimize such interpretive errors, the $\hat{S}_{2D}^{F++}$ representation is recommended for plotting both experimental and calculated 2D spectra.

VI. Conclusions

In this paper, four-level 2D spectra in the Bloch dephasing limit were calculated using the response function of a dimer and parameters appropriate to carbonyl stretching vibrations. A 3DFT algorithm was applied to simulate propagation, detection, and beam geometry effects in a multilevel system that addresses the experimental distortion of the cross peaks. It is predicted that periodic phase twist in the 2D spectra is present in spectrally resolved pump−probe transients and likely sensitive to coherence transfer processes. Absorptive and dispersive pulse propagation effects reduce the phase twist of peaks in the 2D spectra, mimicking a signature of coherence transfer. Further, the directional filtering effect from a noncollinear beam geometry accounts for some unequal cross peak intensities in experimental 2D spectra. We present a transformation to correct for beam geometry distortion wherein excitation frequencies, ω_a and ω_b are substituted by ω_τ, and the excitation frequency ω_c by the detection frequency ω_t. (ω_τ and ω_t are the experimentally accessible parameters.) If we combine the suggested transformation to correct for beam geometry effects with the previously presented transformation to correct for beam propagation and dispersion distortions, the new representation of the 2D spectrum $\hat{S}_{2D}^{F++}$ matches the ideal 2D spectrum within the convergence error when all coherence has decayed. Even in the presence of coherence, the performance of the combined transformation, which is not exact, is remarkably good; the new representation, S_{2D}^{F++} reduces the error in the 2D spectrum by a factor of 4.

Acknowledgment. This work was supported by the National Science Foundation. M.K.Y. and E.R.S. were partly supported by NSF IGERT traineeships through the Optical Science and Engineering Program. We thank Munira Khalil for helpful comments on the manuscript. D.M.J. thanks Robert W. Field for introducing him to double resonance in 1985, for mentoring his Ph.D. thesis, and for enthusiastic support and encouragement ever since.

References and Notes

(1) Aue, W. P.; Bartholdi, E.; Ernst, R. R. *J. Chem. Phys.* **1976**, *64*, 2229.
(2) Ernst, R. R.; Bodenhausen, G.; Wokaun, A. *Principles of Nuclear Magnetic Resonance in One and Two Dimensions*; Oxford University Press: Oxford, 1987.
(3) Hybl, J. D.; Albrecht, A. W.; Faeder, S. M. G.; Jonas, D. M. *Chem. Phys. Lett.* **1998**, *297*, 307.
(4) Zhang, W. M.; Chernyak, V.; Mukamel, S. *J. Chem. Phys.* **1999**, *110*, 5011.
(5) Hybl, J. D.; Ferro, A. A.; Jonas, D. M. *J. Chem. Phys.* **2001**, *115*, 6606.
(6) Hybl, J. D.; Christophe, Y.; Jonas, D. M. *Chem. Phys.* **2001**, *266*, 295.
(7) Zanni, M. T.; Hochstrasser, R. M. *Curr. Opin. Struct. Biol.* **2001**, *11*, 516.
(8) Zanni, M. T.; Ge, N. H.; Kim, Y. S.; Hochstrasser, R. M. *Proc. Natl. Acad. Sci. U.S.A.* **2001**, *98*, 11265.
(9) Demirdoven, N.; Khalil, M.; Tokmakoff, A. *Phys. Rev. Lett.* **2002**, *89*, 237401.
(10) Jonas, D. M. *Annu. Rev. Phys. Chem.* **2003**, *54*, 425.
(11) Khalil, M.; Demirdoven, N.; Tokmakoff, A. *J. Phys. Chem. A* **2003**, *107*, 5258.
(12) Khalil, M.; Demirdoven, N.; Tokmakoff, A. *Phys. Rev. Lett.* **2003**, *90*, 047401.
(13) Jonas, D. M. *Science* **2003**, *300*, 1515.
(14) Tian, P. F.; Keusters, D.; Suzaki, Y.; Warren, W. S. *Science* **2003**, *300*, 1553.
(15) Khalil, M.; Demirdoven, N.; Tokmakoff, A. *J. Chem. Phys.* **2004**, *121*, 362.
(16) Cowan, M. L.; Ogilvie, J. P.; Miller, R. J. D. *Chem. Phys. Lett.* **2004**, *386*, 184.
(17) Hamilton, C. E.; Kinsey, J. L.; Field, R. W. *Annu. Rev. Phys. Chem.* **1986**, *37*, 493.
(18) Bloembergen, N. *Nonlinear optics*; W Benjamin: New York, 1965.
(19) Mukamel, S. *Principles of Nonlinear Optical Spectroscopy*; Oxford University Press: New York, 1995.
(20) Mukamel, S.; Abramavicius, D. *Chem. Rev.* **2004**, *104*, 2073.
(21) Belabas, N.; Jonas, D. M. *Opt. Lett.* **2004**, *29*, 1811.
(22) Belabas, N.; Jonas, D. M. *J. Opt. Soc. Am. B* **2005**, *22*, 655.
(23) Yetzbacher, M. K.; Belabas, N.; Kitney, K. A.; Jonas, D. M. *J. Chem. Phys.* **2007**, *126*, 044511.
(24) Keusters, D.; Warren, W. S. *J. Chem. Phys.* **2003**, *119*, 4478.
(25) Keusters, D.; Warren, W. S. *Chem. Phys. Lett.* **2004**, *383*, 21.
(26) Kumar, K.; Sinks, L. E.; Wang, J. P.; Kim, Y. S.; Hochstrasser, R. M. *Chem. Phys. Lett.* **2006**, *432*, 122.
(27) Bloembergen, N.; Pershan, P. S. *Phys. Rev.* **1962**, *128*, 606.
(28) Allen, L.; Eberly, J. H. *Optical Resonance and Two-Level Atoms*; Dover: New York, 1987.
(29) Kubo, R. *Adv. Chem. Phys.* **1969**, *15*, 101.
(30) Klauder, J. R.; Anderson, P. W. *Phys. Rev.* **1962**, *125*, 912.
(31) Yan, Y. J.; Mukamel, S. *J. Chem. Phys.* **1988**, *88*, 5735.
(32) Tanimura, Y.; Mukamel, S. *Phys. Rev. E* **1993**, *47*, 118.
(33) Gu, Y. G.; Widom, A.; Champion, P. M. *J. Chem. Phys.* **1994**, *100*, 2547.
(34) Gallagher Faeder, S. M.; Jonas, D. M. *J. Phys. Chem. A* **1999**, *103*, 10489.
(35) Engel, G. S.; Calhoun, T. R.; Read, E. L.; Ahn, T. K.; Mancal, T.; Cheng, Y. C.; Blankenship, R. E.; Fleming, G. R. *Nature* **2007**, *446*, 782.
(36) Collini, E.; Scholes, G. D. *J. Phys. Chem. A* **2009**, *113*, 4223.
(37) Faeder, S. M. G.; Jonas, D. M. *Phys. Rev. A* **2000**, *62*, 033820.
(38) Sung, J. Y.; Silbey, R. J. *J. Chem. Phys.* **2003**, *118*, 2443.
(39) Smith, E. R.; Farrow, D. A.; Jonas, D. M. *J. Chem. Phys.* **2005**, *123*, 044102.
(40) Hu, Y. Z.; Koch, S. W.; Lindberg, M.; Peyghambarian, N.; Pollock, E. L.; Abraham, F. F. *Phys. Rev. Lett.* **1990**, *64*, 1805.
(41) Mills, I. M.; Robiette, A. G. *Mol. Phys.* **1985**, *56*, 743.
(42) Lehmann, K. K.; Coy, S. L. *J. Chem. Soc., Faraday Trans. 2* **1988**, *84*, 1389.
(43) Yariv, A. *Quantum Electronics*; Wiley: New York, 1975.
(44) Shen, Y. R. *The Principles of Nonlinear Optics*; Wiley-Interscience: New York, 2002.
(45) Merchant, K. A.; Thompson, D. E.; Fayer, M. D. *Phys. Rev. Lett.* **2001**, *86*, 3899.
(46) Bax, A.; Freeman, R. *J. Magn. Reson.* **1981**, *44*, 542.
(47) Blatt, J. M.; Weisskopf, V. F. *Theoretical Nuclear Physics*; Dover: New York, 1991.
(48) Qian, W.; Jonas, D. M. *J. Chem. Phys.* **2003**, *119*, 1611.
(49) McClain, W. M. *J. Chem. Phys.* **1971**, *55*, 2789.
(50) Ferro, A. W. A.; Hybl, J. D.; Faeder, S. M. G.; Jonas, D. M. *J. Chem. Phys.* **2001**, *115*, 5691.
(51) Cheng, Y. C.; Fleming, G. R. *J. Phys. Chem. A* **2008**, *112*, 4254.
(52) Kano, H.; Kobayashi, T. *Opt. Commun.* **2000**, *178*, 133.
(53) Tekavec, P. F.; Myers, J. A.; Lewis, K. M.; Ogilvie, J. P. *Opt. Lett.* **2009**, *34*, 1390.
(54) Milota, F.; Sperling, J.; Nemeth, A.; Kauffmann, H. *Chem. Phys.* **2009**, *357*, 45.
(55) Nee, M. J.; Baiz, C. R.; Anna, J. M.; McCanne, R.; Kubarych, K. J. *J. Chem. Phys.* **2008**, *129*, 084503.
(56) Farrow, D. A.; Smith, E. R.; Qian, W.; Jonas, D. M. *J. Chem. Phys.* **2008**, *129*, 174509.

JP904504Z